Interpretation of the Na^+ Ionic Conductivity in $Na_4P_2S_{7-x}O_x$ Mixed Oxy-Sulfide (MOS) Glasses: Effects of Oxygen Doping

Authors and Affiliations

Steven Kmiec, Madison Olson, Matthew Kenney, Steve W. Martin*

Department of Materials Science & Engineering

Iowa State University of Science & Technology

Ames, IA 50011

Abstract

Many researchers around the world are working to make the numerous advantages, safety and energy density the most important, of all-solid-state-batteries a marketplace reality. Chief among these challenges are to develop new solid electrolytes that are highly conducting yet chemically and electrochemically stable at high and low voltages. New mixed oxy-sulfide (MOS) glassy solid electrolytes (GSEs) have been developed recently in this effort to improve upon pure sulfide GSEs which are notoriously chemically and electrochemically unstable. The addition of oxygen dramatically improves the chemical and electrochemical stability of pure sulfide GSEs but decreases the ionic conductivity. In this study, new MOS $Na_4P_2S_{7-x}O_x$, $0 \leq x \leq 5$ GSEs, (NPSO GSEs) were prepared by the melt quench (MQ) technique to develop a better understanding of the exact causes for the decrease in the ionic conductivity with added oxygen in MOS GSEs. As expected, with the incorporation of oxygen, the sodium ion conductivity generally decreases and the average activation energy generally increases. However, as has been found in other MOS

* Corresponding author, Email: swmartin@iastate.edu, phone: 515-294-0745

GSEs, at the dilute limit of oxygen, here for values of $0 < x < 1.5$, the conductivity increases and the activation energy decreases producing a local maximum and minimum, in the conductivity and activation energy, respectively. This behavior is associated with a corresponding local maximum in the molar free-volume of the GSE in this same compositional range. The Christensen-Martin-Anderson-Stuart (CMAS) model was used for the first time on MOS GSEs to provide insight into how the covalent (volumetric strain) and ionic (Coulombic) parts of the conductivity and activation energy are affected by the mixing of sulfur and oxygen anions in this these MOS invert glasses. To accurately model the volumetric strain energy in these glasses, it was necessary to carefully analyze the changing coordination environments of the Na^+ cations. In sulfide rich glasses, sodium is predominantly in tetrahedral (T) coordination (NaS_4), while in oxide rich glasses, sodium is found in the trigonal bipyramidal (TBP) coordination (NaO_5). The CMAS calculated activation energies agree to within 10% of the measured experimental values with no adjustable parameters. Similarly to all previously studied GSEs, it was found that the Coulombic forces appear to dominate the activation energy and this behavior suggests that these glasses can be considered "weak" electrolytes where the mobile Na^+ ions are for the most part ionically bound charges conducting by a "rattle and jump" mechanism where the resident time between jump events is long compared to the mobile cation jump event time. The increase in the Coulombic binding energy part, ΔE_B, of the conductivity activation energy, $\Delta E_{act} = \Delta E_B + \Delta E_S$, where ΔE_S is the volumetric strain part, is found to be the root cause for the overall increase in ΔE_{act} and the concomitant overall decrease in the Na^+ conductivity of the NPSO GSEs.

Introduction

Many researchers around the world are working to make the numerous advantages, safety and energy density the most important, of all-solid-state-batteries a marketplace reality. Chief among these challenges are to develop new solid electrolytes that are highly conducting yet chemically and electrochemically stable at high and low voltages. While solid state electrolyte (SSE) research has been active for nearly two hundred years, much research still needs to be done to find new sodium-based SSEs that can meet the many rigorous requirements necessary for their applications in all solid-state sodium batteries. Such all solid-state sodium batteries are actively being considered for grid scale energy storage applications.[1-7] Specifically, an optimized SSE should exhibit a Na^+ ionic conductivity $>10^{-4}$ $(\Omega\ cm)^{-1}$ at 25 °C, be stable at low potential, ~0 V vs. Na/Na^+, and at high potential, ~4 V vs. Na/Na^+, be a fully dense and monolithic sheet to suppress dendrite growth, and be easily processed at scale in low cost.[8-13] To date, no SSEs achieve all of these criteria simultaneously; but many come close, including sodium beta alumina, NASICON type materials, and more recently sulfide materials and anti-perovskites[14-21].

Glassy solid electrolytes (GSEs), especially pure sulfide GSEs, have been long considered as possible candidates for all solid-state sodium batteries due to their high ionic conductivity, lack of grain boundaries, wide compositional ranges, and potentially low cost processing[22]. However, they suffer from atmospheric reactivity and electrochemical instability with electrode materials. Recently, mixed oxy-sulfide (MOS) glasses have been shown to deliver the optimal blend of the high ionic conductivity of sulfide-based GSEs and the chemical and electrochemical stability of oxide-based GSEs[22]. While pure oxide GSEs such as the ubiquitous $Na_2O + SiO_2$ are known to be chemically and electrochemically stable in contact with Na metal, these pure oxide GSEs have

room temperature ionic conductivities no greater than 10^{-9} $(\Omega\ cm)^{-1}$, which is five orders of magnitude too low, see for example[23-24].

To better understand the exact chemical and electrochemical effects on the Na^+ ionic conductivity of added oxygen to a base pure sulfide GSE to form a MOS GSE, we have investigated one of the simplest perhaps archetypical sodium sulfide-based GSEs, $Na_4P_2S_7$ and its oxygen doped MOS analogues $Na_4P_2S_{7-x}O_x$ (NPSO) GSEs. This composition has the highest Na/P ratio in the binary $Na_2S + P_2S_5$ system that is both a known congruent compound, and can therefore be more easily structurally analyzed, and yet is still strongly glass forming using standard melt quenching (MQ) techniques. The high Na/P ratio will enable the highest Na^+ conductivity in this GSE series, while the congruent compound structure of this phase will afford simpler structure to conductivity relationships. Its strong glass forming character will afford the facile study of the GSEs in this series with high S to O substitution. Oxygen was incorporated according to this compositional series according to Eq. (1):

$$(2/3)Na_2S+(1/3)[(1-x)P_2S_5+xP_2O_5] = Na_4P_2S_{7-x}O_x \qquad \text{Eq. 1}$$

where oxygen is directly substituted for sulfur with increasing x. This system provides a unique opportunity to understand the properties of these MOS GSEs, and thereby provide a careful study of the effects of the isoelectric substitution of sulfur by oxygen on the Na^+ ionic conductivity. The overall study provides new insights into the mixed anion effect on the ionic conductivity of not only the NPSO GSEs reported here, but all MOS GSEs.

Ionic Conduction in GSEs

The ionic conductivity (σ) in GSEs are typically known to follow the Arrhenius relationship given in Eq. 2, where the temperature-dependent conductivity is controlled most strongly by the activation energy (ΔE_{act}) for ion hopping and the pre-exponential factor (σ_0). This Arrhenius behavior is obeyed for these GSEs in the temperature range of interest here, T > 0 °C.

$$\sigma(T) = \frac{\sigma_0}{T} \exp\left(\frac{-\Delta E_{act}}{RT}\right) \quad \text{Eq. 2}$$

Effects of Volumetric Strain (Covalent) and Collective Coulombic (Ionic) Forces

Martin *et al.*[25] investigated the conductivity in the mixed glass former GSE system Na B Si O using the Christensen-Martin-Andersen-Stuart (CMAS) model and found that certain glass structure short range order (SRO) species contributed to the negative non-linear behavior, the so called negative mixed glass former effect, in the activation energy. In this approach, the ionic conductivity was expressed as the standard expression Eq. 3, which gives the ionic conductivity as functions of the concentration of mobile charge carriers (n), ionic charge (Z), the charge of an electron (e^-), and mobility of the charge carriers (μ). In pure Na^+ conductors, Z and e are constant, resulting in the dependence of the conductivity only on the concentration of mobile ions and their mobility.

$$\sigma_{ionic} = nZe\mu \quad \text{Eq. 3}$$

In turn, both the concentration of mobile ions $n(T)$ and their mobility $\mu(T)$ are also Arrhenius in their temperature dependence as shown in Eqs. 4 and 5 [26-28].

$$n(T) = n_0 exp\left(\frac{-\Delta E_B}{RT}\right) \quad \text{Eq. 4}$$

$$\mu(T) = \mu_0 exp\left(\frac{-\Delta E_S}{RT}\right) \quad \text{Eq. 5}$$

Combining Eqs. 2, 4 and 5, the activation energy (ΔE_{act}) given in Eq. 2, can be expressed as the sum of the Coulombic binding energy (ΔE_B) and the strain energy (ΔE_S) given in Eq. 6.

$$\Delta E_{act} = \Delta E_B + \Delta E_S \quad \text{Eq. 6}$$

Given the wide distribution of SRO species and the varying ionic forces present between the negatively charged SRO species and the positively charged mobile Na^+ cations in these MOS glasses, multiple conduction pathways of varying energy barriers are expected to exist within these MOS GSEs and thereby contribute to a distribution of activation energies for ion hopping.[29] Therefore, the value of ΔE_{act} given above must be considered as the average of the distribution of activation energies the mobile Na^+ experience in their conduction events.

In this work therefore, we seek to carefully investigate the effects of substituting sulfur by oxygen on the activation energies of a prototypical and simply constituted, yet strongly glass forming NPSO GSE series. Here, we have combined detailed compositional studies of the key physical properties, volumetric, mechanical, dielectric and conductive, to construct a model that accurately describes the ionic conduction behavior in these invert MOS glasses for the very first time. The ΔE_{act} values of the NPSO GSEs were evaluated using the short range order (SRO) CMAS model to separately calculate the contributions of ΔE_B and ΔE_S. The increase in the ΔE_B, the Coulombic, part of the conductivity activation energy is found to be the root cause for the overall decrease in the Na^+ conductivity of the NPSO GSEs. While Na^+ ion diffusion is a long range

process and as such longer range elements of the structure must be involved in the ion dynamics, using only the SRO CMAS modeling and a careful attention to the details of the structural changes at the short range, we find that the conductivity activation energy can be accurately calculated in these glasses to an accuracy of greater than 90% without any adjustable parameters. If there are long range effects, the dominant part of the activation energy can be accounted for with knowledge of the 1st coordination sphere only, the SRO. Indeed, this modelling is consistent with the well-known "rattle a long time" and "jump infrequently" model for the these relatively modest Na^+ conductivity glasses.

Experimental methods

Sample Preparation

Bulk disk samples of NPSO GSE compositions were prepared following methods described by Kmiec *et al.*[30] in a N_2 glovebox using as-received sodium sulfide (Na_2S 99.9% Alfa Aesar), phosphorous pentasulfide (P_2S_5, 99.95% Sigma Aldrich), and phosphorous pentoxide (P_2O_5, 99.95% Fisher Scientific). 2 to 3 mm thick glass samples were cast onto a preheated mold set to ~35 °C below the T_g, annealed for approximately 3 hours, and then cooled to room temperature at a rate of 1 °C/min. Samples used for impedance spectroscopy (IS) measurements were dry polished to ~1 μm and gold contact electrodes, 10 mm diameter, were sputtered on the samples using an Anatech Hummer VI Sputtering System located inside the glove box.

Physical Properties

Density Measurements – Archimedes' Method

Density measurements were made inside an Argon glovebox, < 1 ppm H_2O and O_2, on polished MQ samples using the Archimedes' method. Mineral oil with a density of 0.83 g/cm^3 ±0.01 g/cm^3 was used as the immersion fluid. Tests on density standards showed this technique to yield densities with an accuracy and precision of ±0.03 g/cm^3.

Molar Volume, Ionic Volume, and Free Volume Determination

The molar volume (V_m) was calculated from the measured density (ρ) and the formula weight (FW) of the composition using Eq. 7. The ionic volume (V_{ionic}) was calculated for each glass through Eq. 8 using the Shannon ionic radii[31] for the different elements present in the glass. The apparent free volume (V_f) of the glasses was calculated with Eq. 9, by the difference of the V_m and V_{ionic}.

$$Molar\ Volume \equiv V_m(x) = \frac{FW(x)}{\rho(x)} \quad \text{Eq. 7}$$

$$Ionic\ \ Volume \equiv V_{ionic}(x) = \sum_i \left(\frac{4}{3}\pi r_i^3 \right) Z_i(x) \quad \text{Eq. 8}$$

$$Free\ \ Volume \equiv V_f(x) = V_m(x) - V_{ionic}(x) \quad \text{Eq. 9}$$

Mechanical Properties

Longitudinal and Transverse Sound Velocity Measurements

Longitudinal and transverse sound velocities were measured using an Ultratek EUT3160 Pulser/Receiver equipped with 30 MHz and 20 MHz delay line transducers using Vaseline and Salol as coupling agents for longitudinal and transverse waves, respectively. The wave speed was determined using Eq. 10, the experimentally measured thickness of the sample, d, (±0.01 mm), wave echo time, t, (±0.001 s), and a brass sound velocity standard (±50 m/s).

$$v = \left(\frac{2d}{t} \right) [\text{m/s}] \qquad \text{Eq. 10}$$

Young's Modulus, Shear Modulus, Bulk Modulus, and Poisson's ratio

The mechanical properties of the NPSO GSEs were calculated from the experimentally measured longitudinal sound velocity (v_L, m/s), transverse sound velocity (v_T, m/s), and density (ρ, g/cm^3) (±0.03 g/cm^3) using the standard expressions Eqs. 11-15 given in Table 1.

Dielectric Impedance Spectroscopy

Ionic Conductivity and Activation Energy

The equivalent circuit model used to analyze the electrical response of these NPSO GSEs is comprised of series combination of two parallel resistor (R) / constant phase element (CPE) circuits (R||CPE) and a Warburg element (W) and given in Fig. 4B, below. The two R||CPE circuits were used to model the combined conductive and dielectric response of the NPSO GSEs and the GSE-Au electrode interface. The Warburg element was used to model the space charge

polarization behavior that occurs with Na^+ pileup at the Au blocking electrodes, especially at the low frequencies and high temperatures used here.

The ionic conductivity of the NPSO GSEs were measured using a Novocontrol 2 Dielectric spectrometer equipped with a cryostat capable of variable temperature IS measurements between -100 °C and 300 °C (± 0.5 °C). Samples were measured using a custom, airtight sample holder to prevent unwanted reactions with O_2 or H_2O during the measurements. The complex impedance of the samples was measured from 3MHz to 0.1Hz at temperatures ranging from 0 °C to 150 °C. The ionic conductivity was determined by fitting the complex IS plot using the three-component equivalent circuit model described above. Extracting the temperature dependent $R_{bulk}(T)$ from the fitted circuit model, the temperature dependent ionic conductivity was calculated using Eq. 16, where t and A are the sample thickness and electrode area, respectively.

$$\sigma_{d.c.} = \frac{1}{R_{Bulk}(T)}\left(\frac{t}{A}\right) [\Omega cm]^{-1} \qquad \text{Eq. 16}$$

The average activation energy at high temperatures (ΔE_a) for T > 0°C was determined from the temperature dependent conductivity using the Arrhenius relationship given above in Eq. 2.

High Frequency Low Temperature Permittivity Measurements

The limiting high frequency permittivity (ε_∞) values, needed for the CMAS modelling, see below, were measured using the Novocontrol 2 Dielectric Spectrometer and taken as the real permittivity (ε') at 3 MHz measured at -50 °C on the NPSO GSEs. It was shown that -50 °C was sufficiently cold to effectively freeze out Na^+ conduction contributions to the relative permittivity. To ensure accurate permittivity measurements, the sample holder was calibrated with a Teflon standard, $\varepsilon_\infty = 2.1$, to determine the stray capacitance of the sample holder.

Results

Physical Properties

Density, Molar Volume, Ionic Volume, and Free Volume of the NPSO GSEs

The composition dependent density $\rho(x)$ and molar volume $V_m(x)$ for the NPSO GSEs are given in Table 2 and Fig. 1A. The pure sulfide glass (x = 0.0) has a density of 2.00 g/cm^3 (±0.03), which is in good agreement with reported values of 2.01 g/cm^3 for $Na_4P_2S_7$ glass samples prepared via hot pressing and 2.03 g/cm^3 for bulk glass samples[32-33]. With the initial incorporation of oxygen to the series, the $\rho(x)$ decreases to 1.94 g/cm^3 (x = 0.5), before steadily increasing to a maximum of 2.26 g/cm^3 at x = 5.0 with further additions of oxygen. Although glasses with x > 5, such as $Na_4P_2O_7$, cannot be formed as a MQ GSE, to report the complete sulfide to oxide compositional range, the density of the crystalline phase $Na_4P_2O_7$ is 2.53 g/cm^3 (x = 7.0) is given in Table 2 and plotted in Fig. 1a.[34] The $V_m(x)$ values, Table 2 and Fig. 1B, were calculated using Eq. 7 and reveal a near linear decrease as sulfur anions are replaced by oxygen, decreasing from 47.8 mol/cm^3 in the x = 0.0 glass to 33.0 mol/cm^3 in the x = 5.0 composition. Note that these molar volume values were calculated per Na from the formula $1/4[Na_4P_2S_{7-x}O_x] = NaP_{0.5}S_{(7-x)/4}O_{x/4}$

The composition dependence of the ionic volume, $V_{ionic}(x)$, was calculated using Eq. 8, and given in Table 1, and plotted alongside the $V_m(x)$ values in Fig. 1B. $V_{ionic}(x)$ decreases at a constant rate which is found to be proportional to the radius ratio, r_{sulfur}/r_{oxygen}, as expected by the isoelectric substitution of sulfur for oxygen. Unlike $V_m(x)$, $V_{ionic}(x)$ does not exhibit a local maxima at x = 0.5 as perhaps expected from the continuous variation of the composition. Taking the difference between the $V_m(x)$ and the $V_{ionic}(x)$ following Eq. 9, yields the composition dependent free volume

V_f(x), which is given in Table 1 and plotted in Fig. 1C. The V_f of the pure sulfide (x = 0.0) composition was determined to be 17.87 cm^3/mole. Consistent with trends in the density and molar volume described above and what we have seen in the $Li_2S + GeS_2 + GeO_2$ system as reported by Kim *et al.*[35-37], the initial incorporation of oxygen *increased* the V_f to 18.92 cm^3/mole for the x = 0.5 GSE. Like that observed by Kim *et al.* further additions of oxygen, however, steadily decrease V_f, where it reaches a minimum value of ~14 cm^3/mol for the x = 5.0 composition. V_f decreases even further to 12.23 cm^3/mol for crystalline $Na_4P_2O_7$, x = 7. It is significant to note that the extrapolations of the various molar volumes described here agree quite well with those values of polycrystalline $Na_4P_2O_7$. The composition dependent values for the ρ, FW, V_m, V_{ionic}, and V_f are reported in Table 2.

Mechanical Properties

Young's Modulus, Shear Modulus, Bulk Modulus, and Poisson's ratio

The composition dependence of the longitudinal, $v_L(x)$, and transverse, $v_T(x)$, sound velocities are given in Table 3 and Fig. 2A, showing that both sound velocities increase with the addition of oxygen. The $v_L(x)$ is measured to be 3,500 m/s for the pure sulfide (x = 0.0) GSE and steadily increases to ~4,250 m/s for the x = 5.0 GSE. The $v_T(x)$ exhibits a similar trend, increasing from 1750 m/s for the x = 0.0 sample to 2250 m/s for the x = 5 sample. The trend yields values consistent with the values for the pure oxide sodium metaphosphate glass $NaPO_3$ (recall, as described above, $Na_4P_2O_7$ cannot obtained as a homogeneous MQ glass) of v_L = 4,530 m/s and v_T = 2,760 m/s.[38]

The longitudinal (L), bulk (B), shear (G), and Young's (E) modulus were calculated using Eqs. 11-14 and then plotted in Fig. 2B and reported in Table 3. Figure 2B shows that all of the calculated moduli were found to increase gradually in the sulfide-rich glasses, $x < 3$, but increase more rapidly when oxygen becomes the dominant anion, $x \geq 3$. The shear modulus was found to be 6.6 GPa for the pure sulfide glass, which is in good agreement with measurements reported by Nose *et al.*[32] for comparable $Na_2S + P_2S_5$ glasses. With the substitution of ~70% oxygen, the shear modulus was found to approximately double, reaching a value of 12.5 GPa for the x = 5.0 NPSO GSE, see Fig. 3. For comparison purposes, again using the values of the transverse and longitudinal sound velocities for $NaPO_3$ glass as reported by Bhide *et al.*[38], a shear modulus of $NaPO_3$ is found to be 18.8 GPa. The compositionally dependent Poisson's ratio was calculated using Eq. 15 is given in Table 3 and Fig. 2C, showing a small decrease with the incorporation of oxygen.

Dielectric Impedance Spectroscopy

Ionic Conductivity and Activation Energy

The temperature dependent ionic conductivity was measured using complex IS for all of the NPSO GSEs for $T \geq 0$ °C, the range of temperatures expected for applications in ASSSBs. We observed significant and systematic deviation away from strictly Arrhenius behavior in the low temperature range, $T < 0$°C. This behavior, consistent with that we have seen for other compositionally complex glasses like those studied here,[29] arises from the structural disorder of the GSEs and will be reported on separately. As an example, the frequency dependent ionic conductivity, σ_{ac}, for the x = 3.5 NPSO GSE is given in Fig. 4A for $T \geq 0$ °C. The temperature dependent direct current (DC) equivalent resistance (R_{DC}) was determined by fitting each complex

impedance plot, Fig. 4B, at each temperature using the equivalent circuit model shown in Fig. 4B to extract the DC conductivity σ_{DC}(T). Again a few select temperatures are shown in Fig. 4B. The Arrhenius plots for DC conductivity measured in the temperature range T ≥ 0 °C of the NPSO GSEs are given in Fig. 5.

Figure 6 shows the composition dependence of the room temperature ionic conductivity and corresponding activation energy ΔE_{act} with increasing oxygen concentration. The ionic conductivity achieves a maximum $\log(\sigma_{25}) = -5.4\ (\Omega cm)^{-1}$ at the x = 0.5 composition. With further additions of oxygen, the ionic conductivity decreases until reaching $\log(\sigma_{25}) = -7.8\ (\Omega cm)^{-1}$ for the x = 5.0 composition. While it is not completely clear that the data shown in Fig. 6 suggests a maximum in the σ_{25}, the ΔE_{act} values do appear to show a corresponding minima that may be considered slightly larger than the experimental error in measurements. This behavior is consistent with the molar volume measurements shown in Fig. 1 that show a maximum in the free-volume of the glasses at this same composition.

High Frequency Low Temperature Permittivity Measurements

The frequency dependent relative permittivity ε_∞(x) values were measured from 0.1 Hz to 3 MHz at -50 °C and the data for the x = 1.5 NPSO GSE is shown in Fig. S1. As expected for such GSEs, the isothermal relative permittivity decreases strongly with increasing frequency as the mobile ions becomes progressively "frozen out" by the rapidly increasing frequency. Ultimately, the relative permittivity reaches a limiting value ε_∞ where only the much faster bond vibration and atomic polarization mechanisms can contribute to the polarizability of the GSE. Taking this limiting value from the other relative permittivity measurements of the other GSEs in this series, the composition dependence of the limiting high frequency permittivity ε_∞(x) is given in Fig. 7,

showing a general decrease with incorporation of oxygen. Such a decrease is expected from the lower atomic polarizability of the oxygen anion, ~1.8 x 10^{-3} nm^3, compared to that of the sulfide anion, ~5.4 x 10^{-3} nm^3 [39]. The pure sulfide x = 0 GSE exhibited a high frequency permittivity of ~12.5 while the values for the NPSO GSEs decreased to ~10 with increasing concentration of oxygen. Although the magnitude of the change in $\varepsilon_\infty(x)$ is small, ~ 20%, its effect on the ΔE_C has been shown to be quite large[25] and this will be explored carefully below in the analysis of the composition dependence of ΔE_B.

Discussion

Review of the SRO structures of the NPSO GSEs

In order for a careful analysis of the composition dependence of the conductivity and activation energy in these MOS GSEs, we begin with a careful review of the SRO structures of this glass series, which has been determined in a previous study using FTIR, Raman, and ^{31}P MAS NMR spectroscopies[30, 40]. First, from the composition, the expected SRO structure is the P^1 SRO, where the superscript defines the number of bridging sulfurs (BSs) or bridging oxygens (BOs) or a mixture of both. Next, as perhaps might have been expected, the addition of oxygen does not produce a simple homogenous MOS glass network of a mixture of isostructural $PS_{4-y}O_y$ P^1 SRO tetrahedra. Instead, these NPSO GSEs were observed to be comprised of a compositionally dependent mixture of the sulfide ($Na_2PS_{3.5} \equiv P^1$, $Na_2PS_3 \equiv P^{1P}$, and $Na_3PS_4 \equiv P^0$), MOS ($Na_3PSO_3 \equiv P^{0SO}$ and oxide ($NaPO_3 \equiv P^{2O}$ and $NaPO_{3.5}$ P^{1O}) SRO structures. At any x value, compositional balance of charge, [Na^+] = sum of all of the negatively charged SRO anions, and atomic balance of P, O and S were observed.

In the progressive addition of oxygen, x, in these NPSO GSEs the reaction schema given in Eq. 17 was found to generally describe the compositional changes of the various SRO groups in these NPSO GSEs:

$$Na_4P_2S_7 \xrightarrow[-P_2S_5]{+P_2O_5} Na_3PS_{4-y}O_y + NaPO_3 \xrightarrow[-P_2S_5]{+P_2O_5} Na_4P_2O_7 \qquad \text{Eq. 17}$$

This mechanism of incorporation of oxygen is described as a disproportionation reaction where charge and atomic balance are maintained but the various P SRO groups disproportionate into those with larger and smaller numbers of BSs and BOs. In reaction schema Eq. 17, the disproportion reaction can be represented by the reaction: $2P^1 \rightarrow P^0 + P^2$, where the superscript defines the number of BO or BS. In this reaction schema, the sodium ions are redistributed among the various P SRO structures in order to charge balance the newly formed P^0 and P^2 SRO anions. A notable feature of this disproportionation reaction in these NPSO GSEs is its ability to create oligomer $NaPO_3$ oxide chains in the melt, and these have been shown to greatly affect the properties of these glasses as previously reported by Kmiec *et al*[41].

Interpretation of Physical Properties - Density, Molar Volume, and Free Volume

Beyond the local minima at x = 0.5, the density for these $Na_4P_2S_{7-x}O_x$ glasses exhibits a near linear increase with the incorporation of oxygen and the $V_m(x)$ shows a corresponding linear decrease, as shown in Fig. 1A. As defined, the $V_m(x)$ is the sum of the V_{ionic} and the V_f, the V_{ionic} showing an analogous linear decrease with increasing x, shown in Fig. 1B. Although both the $V_m(x)$ and V_{ionic} terms follow nearly linear behavior, Fig. 1B, the V_f, shown in Fig. 1C, exhibits a distinct maximum for the x = 0.5 composition before decreasing with continued addition of

oxygen. Although less apparent, the slight minimum in the density and maximum in the $V_m(x)$ of the sulfide-rich $Na_4P_2S_{7-x}O_x$, x = 0.5 GSEs, are also observed which are associated solely with the observed change in free volume observed in Fig. 1C.

The general change in density and V_{ionic} can be attributed to the overall changes in the various $PS_{4-y}O_y$ SRO tetrahedra present in these glasses as the larger and less dense sulfide tetrahedra (P^{0S}) are replaced by smaller, denser MOS and oxide $PS_{4-y}O_y^{3-}$ SRO tetrahedra. In these invert glasses, the alkali modifiers are so abundant that they not only act as the mobile charge carriers, but also contribute to the amount and nature of the SRO structures formed within the glass.

It has been found that Na^+ ions occupy tetrahedral sites (NaS_4) when coordinated with sulfur[8, 42]. In the oxide analogue, the Na^+ ions are coordinated by five smaller oxygen anions and occupy trigonal bipyramidal sites (NaO_5)[43]. In this NPSO system, small concentrations of oxygen, x < 1, appear to increase the free volume of the GSE. One possible mechanism for this, as described by Kim *et al.*[44] in their studies of MOS Li_2S + GeS_2 + GeO_2 GSEs, could be the formation of mixed tetrahedral [NaX_4; X = O and S] sodium environments. As the concentration of oxygen increases, the oxide species develop a percolating network and transition the sodium environments from tetrahedral to trigonal bipyramidal. We will use this structural hypothesis below to estimate the effect of composition on the various "doorways" accessible to Na^+ as they rattle and jump between local coordination sites.

Mechanical Properties of $Na_4P_2S_{7-x}O_x$ Invert Glasses

Invert glasses, those with more modifier than glass former, differ from traditional covalently-networked glasses in that due to their high modifier content, their network is more

fragmented and is comprised predominately of molecular anions which are bound by ionic forces[45-46]. As such, the mechanical properties of invert glasses are dictated by the dominant ionic, NBX; X = O or S SRO structures present between the minority covalent species. This effect is magnified in sulfide glasses because their ionic and covalent bonds are much weaker than their oxide analogs. Within these MOS glasses, the different bond energies are attributed to the distribution of NBS and NBOs present within the glass. With increasing concentrations of NBOs, the ionic network stiffness increases. Figure 2B shows that the incorporation of oxygen anions into $Na_4P_2S_7$ glass increased the elastic moduli following a power law trend. This is seen especially clearly in Fig. 3, where the data point for the x = 7 $Na_4P_2O_7$ polycrystal is added. For example, the Young's modulus of $Na_4P_2S_7$ is ~ 6 GPa compared to $Na_4P_2O_7$ at ~26 GPa. The factor of >4 increase is associated with the higher field strength of the oxygen anion, as well as the increase in coordination number (CN) of the sodium environment, 4 in the sulfide glass and 5 in the oxide polycrystal.

CMAS Modelling of the Conductivity Activation Energy

The Anderson – Stuart (AS) model was originally proposed to describe the ion transport process in glass, with a focus on relating the conduction process to relevant material parameters though the activation energy[47]. They proposed that the energy barrier for ion transport can be composed of two parts: the Coulombic binding energy (ΔE_B) and the volumetric strain energy (ΔE_S). Although this model has received criticism for its initial assumptions and potential oversimplifications, it does capture key aspects of the ion transport process for a diverse range of glass chemistries. Christensen *et al.*[43] have recently improved upon this in their CMAS model in three ways by correcting a systematic error in the calculation of the cation jump distance, by using the limiting high frequency dielectric permittivity, and by incorporating a structural Madelung

constant (M_C) to describe the ionic network interactions between nearby cations and anions in the glass structure. These corrections were found to accurately predict the activation energy for ion conduction in both covalent oxide and ionic sulfide GSEs[25, 43, 48].

Columbic Binding Energy (ΔE_B) Contribution

In the CMAS model ΔE_B is calculated using Eq. 18 to describe the electrostatic interactions within the glass network of the mobile cations before and after the cation jumps between the various cation sites. ΔE_B can be divided into five parts: 1. The high frequency permittivity (ε_∞), 2. Na^+ and X = O or S geometric constants, $r_{Na}{}^+$ (x), $r_{O}{}^-$ (x), $r_{S}{}^-$ (x), and λ_{cation}, 3. System constants, charge of the Na, O and S, Z_{Na}, Z_o, Z_S, 4. Physical constants, electronic charge (e^-) and permittivity of free-space, and 5. The Madelung constant (M_C). As described by Christensen *et al.* [43] the original A-S model does not have a correct limiting value for zero jump distance, that is $\Delta E_B \rightarrow 0$ as $\lambda \rightarrow 0$ and did not account for many body effects beyond the pairwise coulomb potential of the cation – anion pair. The CMAS model corrects both of these limitations.

$$\Delta E_B(x) = \frac{M_C Z_{Na} Z_X e^2}{4\pi\varepsilon_0\varepsilon_\infty}\left(\frac{1}{r_{Na^+} + r_{X^-}(x)} - \frac{1}{r_{Na^+} + r_{X^-}(x) + \lambda_{cation}/2}\right) \qquad \text{Eq. 18}$$

The variables, necessary to evaluate the different contributions of ΔE_B for the $Na_4P_2S_{7-x}O_x$ GSEs, will be calculated below using experimental data and geometric models.

Strain Energy (ΔE_S) Contribution

The strain energy contribution (ΔE_S) to the activation energy, Eq. 19, originally proposed by McElfresh *et al.*[49] and later modified by Christensen *et al.*[43, 48] consists of four parts: 1. The

shear modulus (G), 2. The corrected jump distance (λ_{cation}), 3. The radius of the mobile cation, r_{Na^+}, and 4. The effective doorway radii (r_D).

$$\Delta E_S = \pi G\left(\frac{\lambda_{cation}}{2}\right)(r_{Na^+} - r_D)^2 \qquad \text{Eq. 19}$$

Martin *et al.*[25], in a study of the invert NaGePS glass system, determined that the ΔE_S generally contributes to < 15% of the overall ΔE_a of the GSEs. This phenomena has also been observed in mixed glass former oxide glasses, Na B P O[43] and Na Si B O[48].

Jump Distance and Free Volume

The composition dependent average jump distance (λ_{cation}) was calculated using Eq. 20 as given by Christensen *et al.*[43], where V_m is the molar volume, N_{Na} is the number of Na ions in one formula unit, N_{glass} is the total number of ions in one formula unit and N_A is Avogadro's number and plotted in Fig. 8. Unlike previous of our studies which were of single anion glasses,[25, 43, 48] the average anion size in this series changes with composition from that of being sulfide dominant to oxide dominant as x increases, which must be considered when describing the ion transport process. The composition dependent average anion radius r_x(x) is therefore defined using Eq. 21, which yields results that are in good agreement with similar studies.[25] The cation jump distance was calculated using the same methods as reported by Christensen *et al.* [38] as given in Eq. 22.

$$\lambda_{cation} = \lambda_{Na} = 2 * \left(\frac{3V_m}{4\pi}\frac{N_{Na}}{N_{glass}}\frac{1}{N_A}\right)^{1/3} \qquad \text{Eq. 20}$$

$$r_{anion} = \left(\frac{x}{7}\right) r_O + \left(\frac{7-x}{7}\right) r_S \quad \text{Eq. 21}$$

$$\lambda/2(\mathrm{x}) = r_{Na^+} + r_{anion}(x) + \lambda_{cation} / 2 \quad \text{Eq. 22}$$

The composition dependent jump distance $\lambda_{cation(x)}$, Fig. 8, calculated from the V_m(x) using Eq. 20, reveals an almost linear decreasing trend with increasing oxygen concentration, decreasing from ~3.6 Å to 3.2 Å. This can be explained by the overall decrease in the molar volume bringing the Na^+ cations closer together caused by the smaller oxygen radius compared to sulfur. However, consistent with the composition dependence of the molar volume that shows a small local maxima at x = 0.5, the jump distance also shows a small, but important, local maximum as well at x = 0.5. We hypothesize that this is associated with the addition of oxygen to the sodium tetrahedral coordination, $NaS_{4-z}O_z$, around the Na^+ in in the sulfide rich end of these compositions as is depicted in Fig. 8. At larger x beyond this local maximum, the average Na-Na jump distance decreases through the formation of the trigonal bi-pyramidal oxide, CN = 5 sodium sites.

Doorway Radius Calculation

The compositionally dependent doorway radius was calculated by generating geometric constructions of the expected Na^+ coordinating sites. It has been shown in sulfide GSEs that Na^+ has a CN = 4 and thus occupies tetrahedral (T) sites[8, 42], while in oxide GSEs the Na^+ have been shown to have a CN = 5, occupying trigonal bipyramidal (TBP) sites[50-52]. Previous studies have shown that the doorway radius can be approximated from the V_m to yield a reasonable value[25, 43]; however, this approximation only holds in single anion systems. Here, to account for the oxygen

and sulfur mixing in these NPSO GSEs, the MOS tetrahedral (NaX_4) and trigonal bi-pyramidal (NaX_5) sites were modeled in a 3D Cartesian coordinate system using unit vectors to describe the atomic positions for any combination of atoms and bond lengths within the tetrahedral and TBP geometries. The window edge lengths (dAB) were calculated by taking the magnitude between the two vectors describing each atomic pair. Each face was then projected onto a 2D plane to define coordinates and radii (rA, rB, etc…) of each atom, creating the windows as given in Fig. 9. Based on the positions and sizes of the three atoms (ions) defining the window, Apollonius' theorem was used to determine the center position[53], producing the largest circle tangent to the window atoms. The radius of the Apollonius circle is the reported doorway radius, r_D, used here in the calculations of the CMAS model for ion conduction. This Apollonius circle is highlighted in Fig. 9 by the inscribed circle within the window defining atoms for NaS_4, NaS_2O_3, and NaO_5 environments. In addition to the doorway radius of each face, the doorway radii of the edge lengths were calculated using Eq. 23 below, to further determine the most likely ion conduction pathway.

$$\text{Edge Doorway Radius} = \frac{dAB - rA - rB}{2} \qquad \text{Eq. 23}$$

The composition dependent doorway radii for all of the tetrahedra environments are given in Fig. 10A, showing an increase in r_D with increasing oxygen concentration. The tetrahedral (NaX_4) – face jump presents the largest of all doorway radii, ~0.8Å, across the sulfur to oxygen transition. The other conduction path from the NaX_4 sites is the edge jump, but this presents a considerably smaller doorway, ranging from 0.45 Å in the NaS_4 site to 0.50Å in the NaO_4 site. From this result, it is clear that the path of least resistance, the smallest ΔE_S, are the face transitions in NaX_4 sites.

Turning to the oxygen dominated (NaX_5) environments, there is larger anisotropy in the potential jump paths of the TBP geometry. Within this configuration, there are three different jump paths that sodium can take, the face, XY-edge, and Z-edge. Using calculations similar to those for the tetrahedral sites, in Fig. 10B, it is seen that the lowest energy barriers in the NaX_5 environments are the face jumps, but with only a 0.07Å difference across the sulfur to oxygen range. Thus, it is fair to assume that if sodium occupies the NaX_5 site, there is an almost equal possibility for Na^+ to hop via the face as the XY-edge.

The doorway radii for all hopping paths are shown in Fig. 11 showing the large differences between the different sodium sites. In order to calculate the strain energy, ΔE_S, the exact manner in which the Na^+ coordination environment changes from NaX_4 to NaX_5 sites with the addition of oxygen must be determined. It is expected that there are systematic changes to the effective doorway radius that will shift as oxygen is added to the glass. Assuming a linear exchange of tetrahedral for TBP sites, the following compositional dependent "effective" doorway radius was determined using Eq. 24 and considers only the lowest energy barrier pathways.

$$Doorway\ Radius(x) = \left(\frac{7-x}{x}\right) r_D(T_{Face}) + \left(\frac{x}{7}\right)\left(\frac{r_D(\mathrm{TBP_{Face}}) + r_D(\mathrm{TBP_{Edge}})}{2}\right) \qquad \text{Eq. 24}$$

Here, it is assumed that the Na^+ will migrate along the path of least resistance (lowest energy barrier) which is dictated in part by the doorway radius. Considering the difference between the calculated T face ($r_D(\mathrm{T_{Face}})$) and T edge ($r_D(\mathrm{T_{Edge}})$) doorway radii of tetrahedra sites, it is reasonable to assume the Na^+ will migrate preferentially via the face hopping mechanism. Sodium ions in TBP sites have a wider range of possible doorway radii to conduct through, however when

considering the sizes of the face, XY_{Edge}, and vertical edge doorway it is clear the $r_D(TBP_{Face})$ and $r_D(TBP_{XY})$ are much larger than the $r_D(TBP_Z)$ pathway as shown in Fig. 12. Thus, both TBP_{Face} and TBP_{XY} are considered as viable pathways for ion migration.

The resulting composition dependence of the effective doorway is given in Fig. 12. By these assumptions, the effective doorway radius decreases essentially linearly with oxygen addition.

Strain Energy Calculation

The activation energy for elastic dilation required strain energy, ΔE_S, calculations which were originally proposed by Frenkel *et al.*[54] as well as by McElfresh and Howitt *et al.*[49], but it wasn't until AS[47] applied it to ion conduction in glasses that a physical model for ion conduction was formed. The AS model was proven to incorrectly predict the ΔE_S by McElfresh *et al.*[49] when they showed more accurate values were calculated by assuming the diffusion barrier behaved like a cylindrical opening as given in Eq. 19, versus a spherical cavity as previously modeled. From these models, it is clear that the strain energy depends most strongly on the $(r_{Na}\text{-}r_D)^2$ term where it grows quadratically as the doorway radius decreases.

The strain energy required for migration via the different doorways present in the $Na_4P_2S_{7-x}O_x$ glasses was calculated using Eq. 19 and values for $G(x)$, $\lambda_{cation}(x)$, and $r_D(x)$ as described above and the values are plotted in Fig. 13. The strain energy is found to be the lowest when Na^+ hop out of sulfide tetrahedral sites via the faces for the x = 0 GSE and largest when hopping out of MOS TBP sites, x = 5. However, the important finding here is that even for the smaller values for r_D for the TBP sites, the ΔE_S values are small, accounting for only ~ 10% over the total conductivity activation energy. Such behavior has been seen before.[25, 43, 48]

Considering the small contribution from the strain energy, the remainder of the paper will focus on the Coulombic binding energy, ΔE_B, which makes up more than 80% the experimental activation energy.

Coulombic Binding Energy Calculation

The Coulombic binding energies, $\Delta E_B(M_C=1)$, where the values of the Madelung constant were first set to 1, i.e. $M_C = 1$, were then calculated using Eq. 18 above and all of the variables described above and these values are shown in Fig. 14. Note that there are no adjustable variables used in Eq. 18, all variables were determined independently of one another and followed from detailed understanding of the structure and physical properties of these GSEs. The total conductivity activation energies for these GSEs were then calculated using Eq. 2, above, and these values are also shown on Fig. 14. These values fall within ~ 10% of the measured conductivity activation energy, ΔE_{act}. The calculations presented here correctly predict the overall trend of an increasing activation energy with oxygen addition. The significantly larger ΔE_B compared to the ΔE_S values suggest that these GSEs, like many studied before, should be considered as weak electrolytes, where the mobile Na^+ are Coulombically bound to their charge compensating cation, sulfur for x = 0 and oxygen for x = 7.[55-57] The increasing trend for the ΔE_B values suggests that the smaller, higher charge density oxygen anions create a larger coulomb binding energy

Consistent with this trend is also the composition dependence of the high frequency permittivity, ε_∞, which decreases with the incorporation of oxygen from 12.5 for the x = 0.0 glass to ~10 for the x = 5.0 composition.

In addition to the cation jump distance, λ_{cation}, and the cation and anion radii, the permittivity, or electronic polarizability, is an important parameter in determining the ΔE_B values,

according to the CMAS model analysis of invert MOS glasses[25, 43, 48]. This is due to the strong dependence that Coulombic binding energy has on the high frequency permittivity, and the almost negligible effect that strain energy contributes to the ΔE_{act} in these GSEs. Small changes in the permittivity result in 10's of kJ/mol changes in the calculated binding energy, however 10's of GPa changes in the shear modulus is necessary to make the strain energy a notable contributor given the calculated doorway radii.

Madelung Constant Approximation

So far in these calculations, the Madelung constant (M_C) has been set to unity and very good agreement has been observed between the CMAS model and the measured ΔE_{act} values. The M_C has been used to describe the long-range electrostatic forces acting on the ions in ionic compounds[25, 58-59]. In general, the M_C is often greater than 1 in ionic salts (as the ion is felt by multiple shells of its local coordination sphere) [57-59]. Within the CMAS model, the M_C is the only adjustable parameter in the model[25, 43]. Here we consider the use of the M_C value.

M_C is a value that describes the cumulative and summative electrostatic interactions from all charges acting on a single charge and summed over all sites in the ionic solid all scaled by the inverse of the distance between the point charge and the distant charge. Hence, the closer point the charges, the larger contribution to M_C. The *Mc* approximation breaks down as it approaches defects or interfaces. Additional problems arise when applying this concept to glassy materials which possess both no long range order and a continual network of defects, however, MacFarlane *et al*. have developed numerical models to calculate the M_C value for molten salt ionic liquids.[60]

Here, the values of the M_C were calculated by using Eq. 25 and these values are shown in Fig. 15. Given the excellent agreement between the calculated value $\Delta E_B + \Delta E_S$ and the

experimentally measured value, ΔE_{act}, shown in Fig. 14, the near unity value of M_C is to be expected. This suggests that relative permittivity ε_∞ may be consider sufficient to account for all of the long range electrostatic shielding effects caused by the glassy network. Not only are the calculated M_C values only slightly larger than unity, but they are also essentially independent of composition. This latter attribute suggests that the CMAS model accurately predicts the underlying chemical changes effecting the conductivity activation energies in these NPSO GSEs.

$$M_C = \frac{\Delta E_{act} - \Delta E_S}{\Delta E_B \left(M_C = 1 \right)} \qquad \text{Eq. 25}$$

Conclusions

This study investigated the underlying reason for the decrease in the ionic conductivity upon the addition of oxygen to the sulfide invert glass, NPSO GSEs using the CMAS model. The activation energy was calculated through the sum of the strain and binding energies. It was determined the activation energy is binding energy dominated, and that the strain energy contributes a small <10% amount. The calculated activation energies agreed to the experimentally measure values to within less than 10%. This agreement was achieved with no adjustable parameters in the model. All of the various parameters and values used in the calculation of the Coulombic and strain energies were either fixed universal constants or calculated directly without approximation from the glass composition and other measurements of the glass structure and properties such as the density and high frequency permittivity. The strong dependence of the conductivity activation energy on the Coulombic binding term can be explained by the high concentration of ionic NBX sites which bind the fragmented covalent species to the continuous

Na^+ matrix, ultimately dictating the network strength. As seen in other MOS GSEs, small additions of oxygen, here x = 0.5, caused a slight expansion in the molar volume of the GSE and this led to a sharp local minimum in the ΔE_{act} of these MOS GSEs.

Supporting Information

Additional information on the values of the room temperature conductivity, the conductivity activation energy, the conductivity pre-exponential factor and the limiting high frequency dielectric relative permittivity for glasses measured in this work.

Acknowledgments

Funding for this work was provided by the ARPA-E of the Department of Energy through contract number DE-AR0000654 and DE-AR-0000778. Additional funding for this work was provided by the Vehicle Technology Office within the Department of Energy though the contract DE-EE0008852, the Iowa Energy Center of the Iowa Department of Economic Development through grant number 307352 and by the National Science Foundation through grant DMR 1936913.

List of Tables

List of Figures

Figure 5. Arrhenius plots of the d.c. Na^+ ionic conductivity of the $Na_4P_2S_{7-x}O_x$ glass compositions in the high temperature, > 298 K, region, showing an increase in the activation energy and a decrease in the d.c. Na^+ ionic conductivity with oxygen additions.

Figure 6. Composition dependence of the d.c. Na^+ ionic conductivity at 298K of $Na_4P_2S_{7-x}O_x$ glasses and the activation energy ΔE_{act} from the Arrhenius fit to Eq. 2.

Figure 7. A. Frequency dependence of the real part of the complex permittivity ε' showing the determination of the high frequency permittivity, ε_∞, measured at T = 223K. B. Composition dependence of ε_∞ of the $Na_4P_2S_{7-x}$ Ox glasses.

Figure 8. Composition dependence of the average Na^+ jump distance, λ_{cation}, determined from the anion distribution in and the molar volume of the glasses. With increasing x, the jump distance decreases as the result of a denser glass network arising from the small oxygen anions.

Figure 9. Two dimensional depictions of the geometric models for the r_D doorway analysis. (Top) The NaS_4 tetrahedral (T) site with a doorway of 3 sulfur atoms, showing a much larger doorway though the face than the edges of the T site. (Left) The $NaSO_4$ trigonal bi-pyramidal (TBP) site with a window consisting of 1 sulfur atom (Vert) and 2 oxygen atoms (XY-edge). The vertical edge (dAC and dBC) exhibits a contracted doorway due to the higher CN and thus it is proposed, see text, that the Na^+ ions prefer to jump via the face or XY edge in the NaX_5 MOS sites. (Right) The NaO_5 site with a window consisting of 3 oxygen atoms, showing a much larger doorway though the face and XY- edges compared to that of the vertical edges.

Figure 10. A. Composition dependence of the calculated face and edge doorway radii, r_D, for the proposed NaX_4 tetrahedral environments showing that both values increase nearly linearly with the addition of oxygen. B. Composition dependence of the calculated face and XY-edge doorway radii, r_D, for proposed NaX_5 trigonal bipyramidal environments showing a sigmoidal increase in both values with the addition of oxygen.

Figure 11. Comparisons of the calculated doorway radii, r_D, for all of the NaX_4 and NaX_5 MOS environments. Both the face and edge doorway radii were calculated from geometric models of the sites using a numerical solution to the Apollonius theorem, see text.

Figure 12. Proposed composition dependence of the doorway radius, r_D, assuming the largest physically reasonable doorways that in turn would result in the lowest strain energies, ΔE_S. Here, a linear exchange between NaX_4 – Face, and the average NaX_5 – (Face + XY(Edge))/2 doorway radii is assumed to account for the coordination number change. Here it is expected that for the x = 0 pure sulfide glass, all of the Na are expected to be coordinated in NaS_4 tetrahedral environments whereas for the x = 7 pure oxide, all of the Na are expected to be coordinated in NaO_5 trigonal bipyramidal environments.

Figure 13. Strain energy contribution as determined by the different jump paths (doorway radii) of the investigated NaX_4 and NaX_5 site geometries.

Figure 14. Calculated composition dependence of the strain energy, ΔE_S, based on the proposed effective doorway radius, Fig. 12, Calculated composition dependence of the binding energy, ΔE_B, and the sum $\Delta E_B + \Delta E_S$ compared to the experimentally measured ΔE_{act} values. The model calculated sum agrees exceptionally well with and within the experimental error of the experimentally determined values. Open symbols refer to the calculated and measured values for the polycrystalline ceramic x = 7, $Na_4P_2O_7$.

Figure 15. Calculated composition dependent Madelung constant, M_C, for the $Na_4P_2S_{7-x}O_x$ glasses from the calculated total of ΔE_B and ΔE_S and the measured activation energy ΔE_{act}, see text. The value of near unity shows that the model calculated total activation energy agrees well with the experimentally determined conductivity activation energy. Such agreement suggests that the many body effects of the coulomb potential appears to well be described by the limiting high frequency ε_∞ values, Fig. 8 B.

Table 1. Equations used to calculate the mechanical modulii and Poisson ratio from the sound velocity and density measurements.

Mechanical Property	***Equation***	***Units***
Longitudinal Modulus (L)	$L = \rho v_L^2$ Eq. 11	Pa
Shear Modulus (G)	$G = \rho v_T^2$ Eq. 12	Pa
Bulk Modulus (K)	$K = L - \frac{4}{3}G$ Eq. 13	Pa
Young's Modulus (E)	$E = (1+\nu)2G$ Eq. 14	Pa
Poisson's Ration (ν)	$\nu = \frac{L-2G}{2(L-G)}$ Eq. 15	-

Table 2. Composition dependence of the density, molar volume, V_{molar}, and calculated molar ionic volume, V_{ionic}, and molar free volume, V_{free} for $Na_4P_2S_{7-x}O_x$ per Na glasses.

x	Density (g/cm^3)	Error ($\pm$ g/cm^3)	Formula Weight (g/mol) per Na	Molar Volume per $NaP_{0.5}S_{(7-x)/4}O_{x/4}$ (cm^3/mol)	Calculated Ionic Volume (cm^3/mol)	Calculated Free Volume (cm^3/mol)
0.0	2.00	0.03	94.59	47.80	29.94	17.87
0.5	1.94	0.02	92.58	47.72	28.80	18.92
1.0	1.98	0.01	90.57	45.75	27.67	18.08
1.5	2.01	0.02	88.57	44.13	26.53	17.60
2.0	2.03	0.01	86.56	42.56	25.40	17.17
2.5	2.04	0.01	84.55	41.48	24.26	17.22
3.0	2.10	0.01	82.54	39.28	23.13	16.15
3.5	2.14	0.02	80.53	37.70	21.99	15.71
4.0	2.17	0.02	78.53	36.15	20.86	15.30
4.5	2.21	0.02	76.52	34.62	19.72	14.90
5.0	2.26	0.01	74.51	33.00	18.59	14.41
7.0	2.53*	0.00	66.48	26.28	14.05	12.23

* The density for x = 7, $Na_4P_2O_7$, is the density of the fully dense polycrystalline ceramic reported in the Materials Project Database[61-62]

Table 3. Ultrasonic sound velocities and calculated mechanical modulii and Poisson's ratio of $Na_4P_2S_{7-x}O_x$ glasses.

x	V_l (m/s)	V_t (m/s)	Shear Modulus (GPa)	Young's Modulus (GPa)	Bulk Modulus (GPa)	Longitudinal Modulus (GPa)	Poisson's Ratio (v)
0	3498	1821	6.6	17.4	15.6	24.4	0.31
1.0	3642	1814	6.5	17.4	17.6	26.3	0.34
2.0	3701	1981	8.0	20.7	17.2	27.9	0.30
3.0	3797	1989	8.3	21.8	19.2	30.3	0.31
4.0	4166	2152	10.1	26.5	24.3	37.7	0.32
4.5	4187	2255	11.2	29.1	23.8	38.7	0.30
5.0	4265	2353	12.5	32.0	24.4	41.1	0.28
*7.0	--	--	23.4	60.0	45.5	--	0.28

* Values reported for $Na_4P_2O_7$ correspond to the crystalline phase and were reported in the Materials Project Database[61-62].

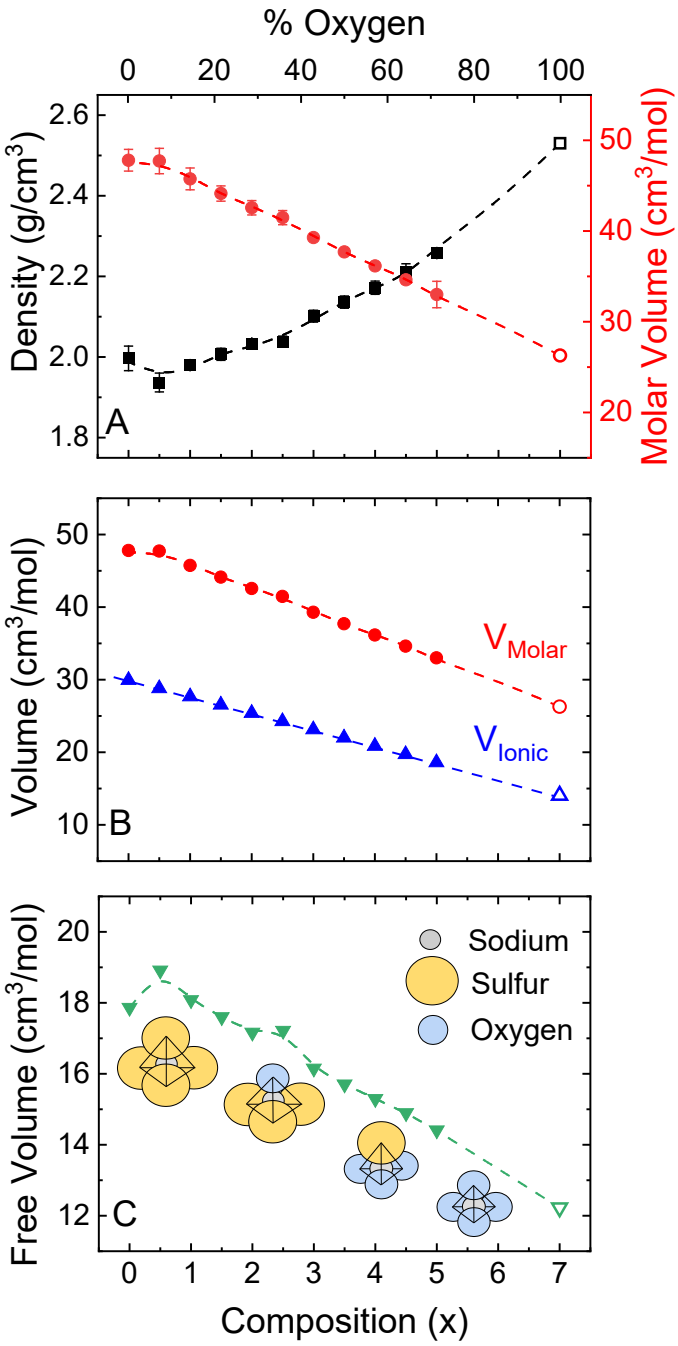

Figure 1. A. Composition dependence of the density and the molar volume of the $Na_4P_2S_{7-x}O_x$ glasses. B. Composition dependence of the molar volume and calculated ionic volume. C. Composition dependence of the free volume $V_{free} \equiv V_{molar} - V_{ionic}$ for $Na_4P_2S_{7-x}O_x$ glasses. The open symbol for x = 7 is for polycrystalline $Na_4P_2O_7$ as reported in the Materials Project Database[61-62].

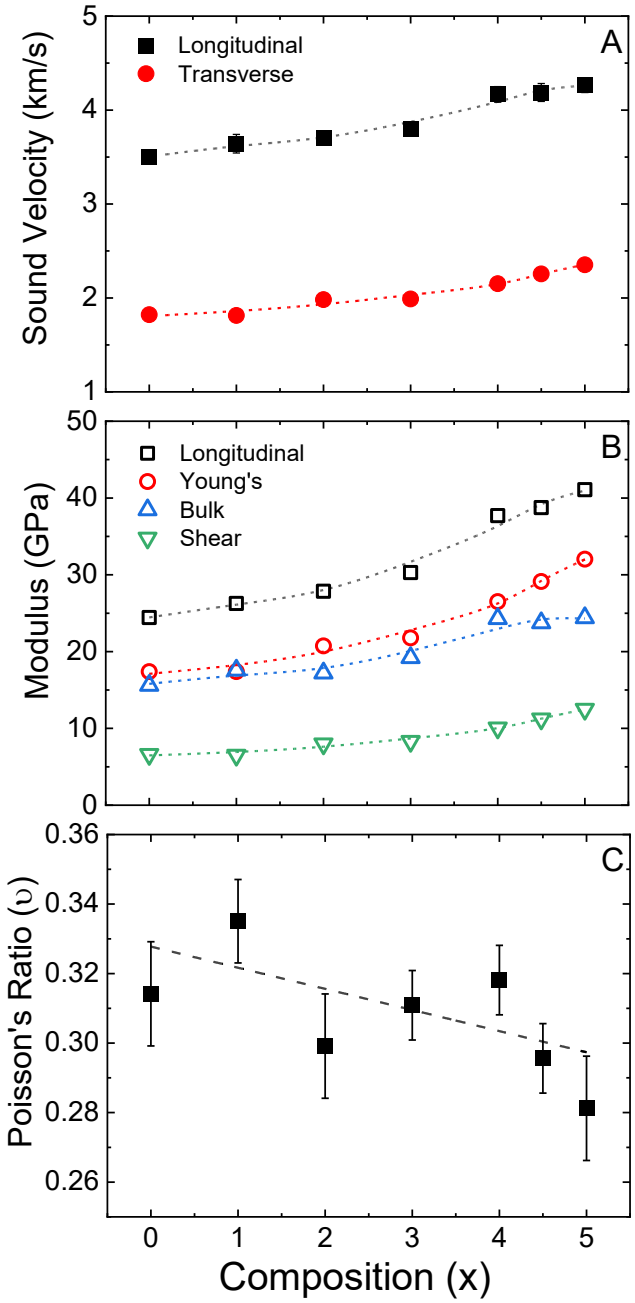

Figure 2. A. Composition dependence of the longitudinal and transverse sound velocities measured on annealed $Na_4P_2S_{7-x}O_x$ glass discs. Error limits for the sound velocity measurements are comparable to the size of the symbol. B. Composition dependence of the calculated mechanical moduli. Error limits for the mechanical moduli are comparable to the size of the symbol. C. Composition dependence of the Poisson's ratio of $Na_4P_2S_{7-x}O_x$ glasses.

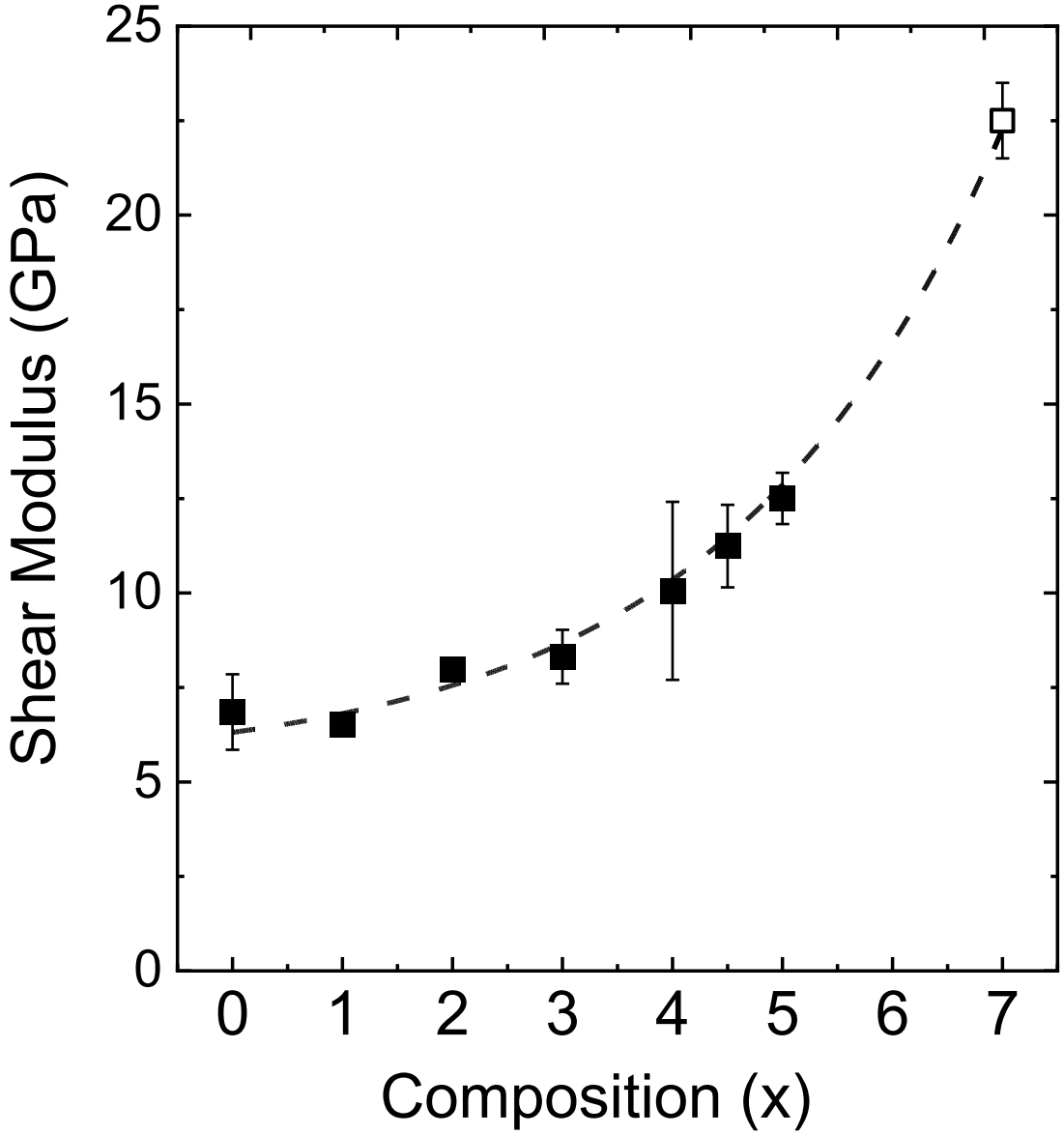

Figure 3. Composition dependence of the shear modulus of the $Na_4P_2S_{7-x}O_x$ glasses exhibiting a non-linear increase as oxygen is incorporated into the glass network. Line is a guide to the eye only. Data point for x = 7 is for polycrystalline $Na_4P_2O_7$ reported in the Materials Project Database[61-62].

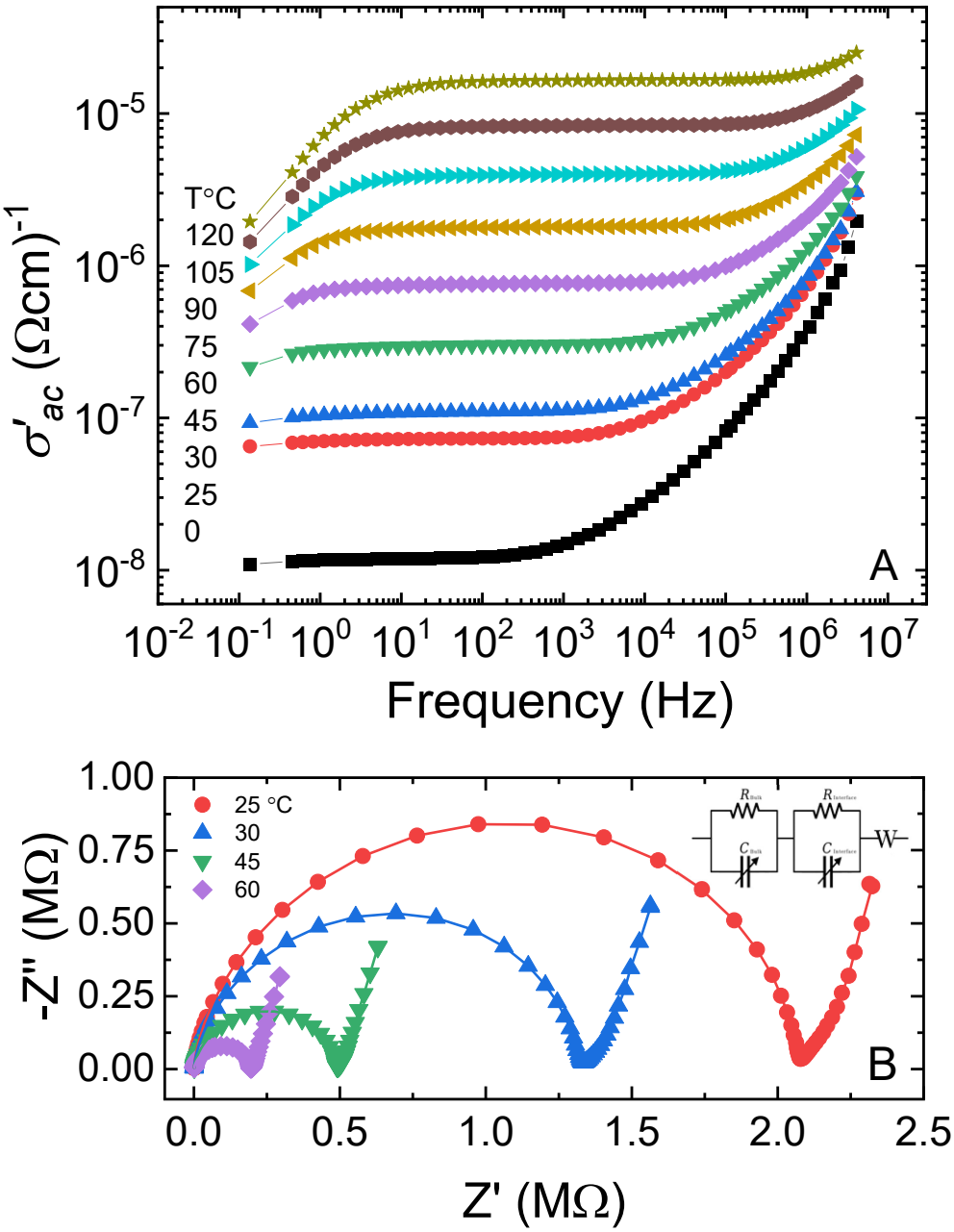

Figure 4. A. EIS frequency sweep (10MHz to 0.1Hz) of the x = 3.5 $Na_4P_2S_{3.5}O_{3.5}$ glass sample for temperatures from 0 °C to 120 °C. B. Example Nyquist plots for a range of temperatures of the x = 0 $Na_4P_2S_7$ glass sample used to extract the R_{bulk} at the various temperatures to calculate the d.c. Na^+ ionic conductivity. The insert to B shows the combined bulk and interfacial (intf.) impedance model used to fit the experimental EIS data.

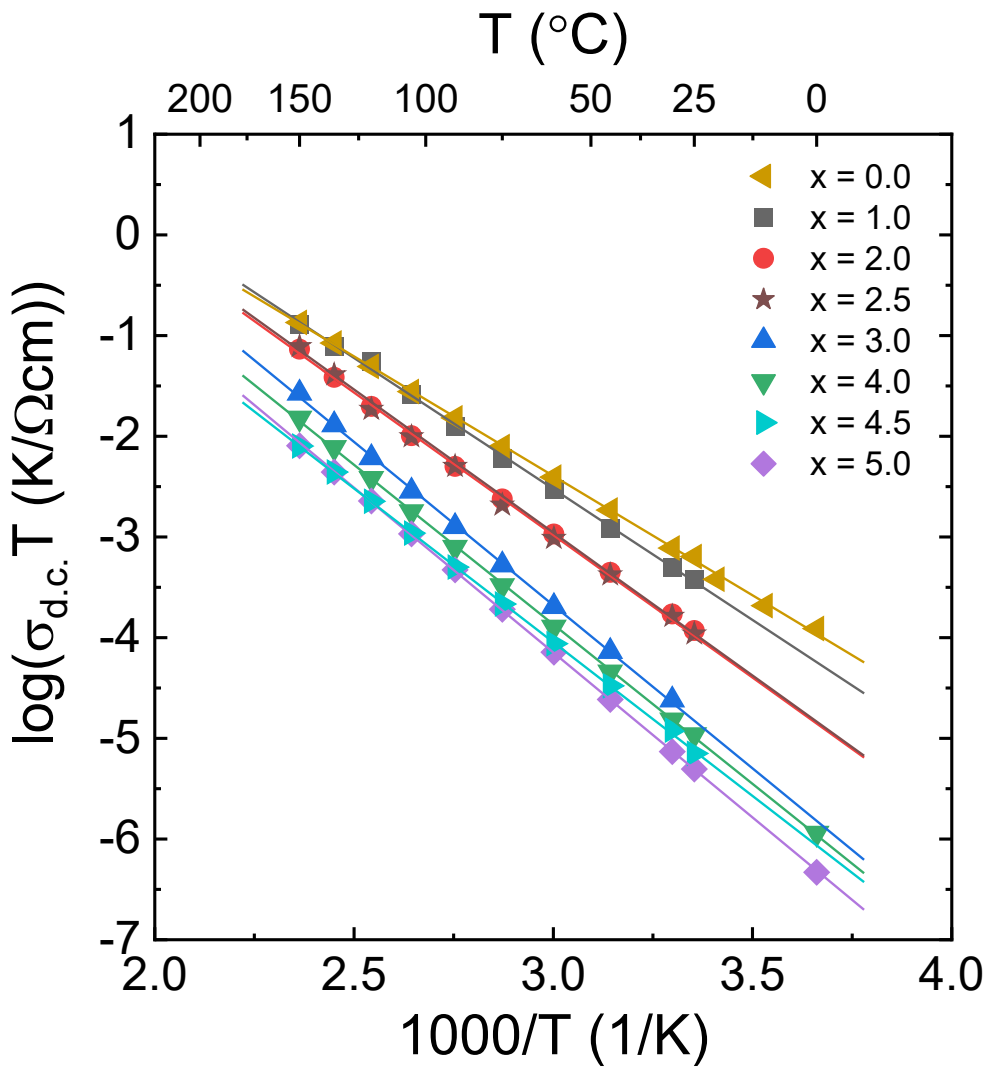

Figure 5. Arrhenius plots of the d.c. Na^+ ionic conductivity of the NPSO GSEs for T ≥ 0 °C showing, in general, an increase in the activation energy and a decrease in the d.c. Na^+ ionic conductivity with oxygen additions.

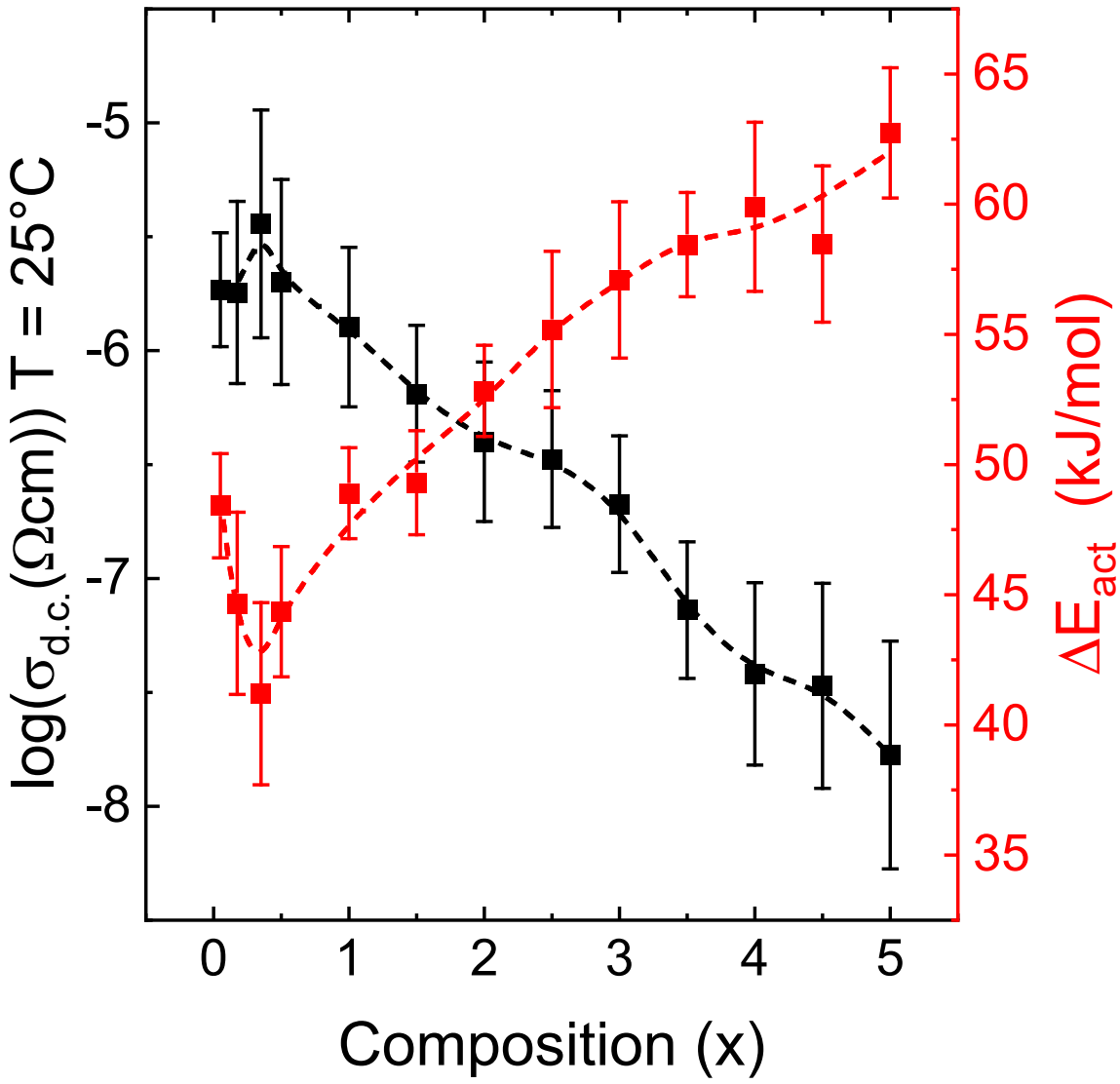

Figure 6. Composition dependence of the d.c. Na^+ ionic conductivity at 298K of $Na_4P_2S_{7-x}O_x$ glasses and the activation energy ΔE_{act} from the Arrhenius fit to Eq. 2.

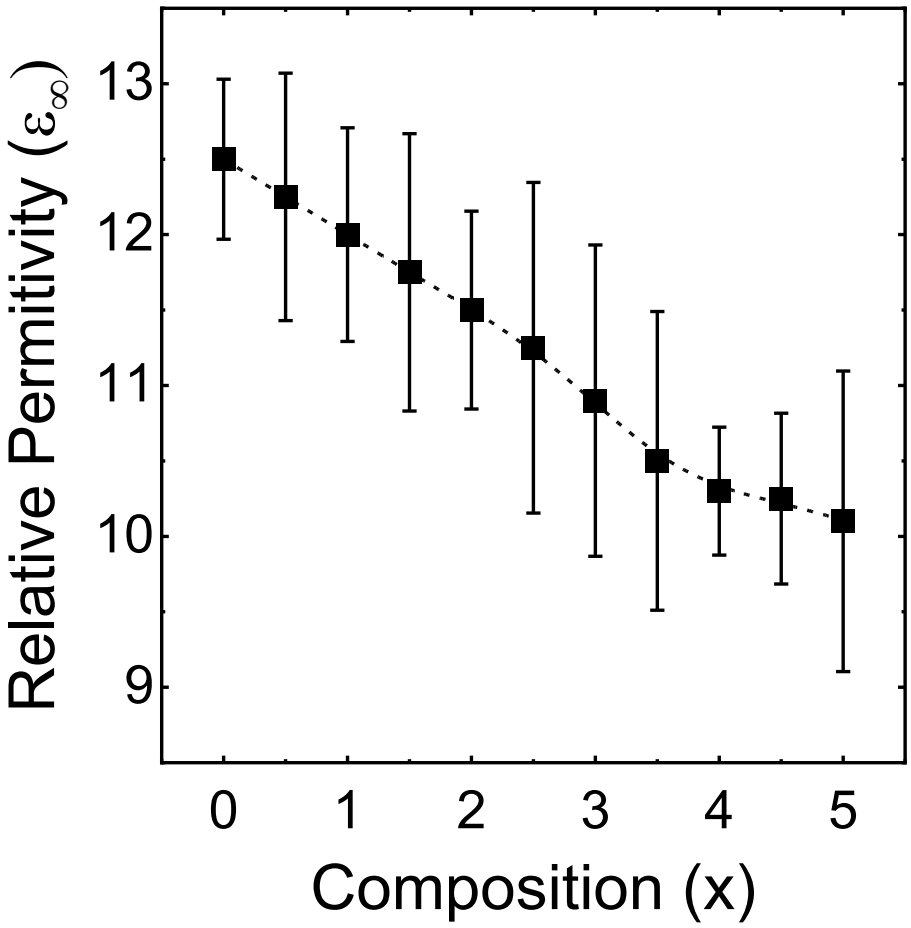

Figure 7. Composition dependence of ε_∞ of the $Na_4P_2S_{7-x}O_x$ glasses. Figure S2 gives an exemplar frequency dependence of the permittivity for the x = 1.5 GSE showing how these ε_∞ values were determined.

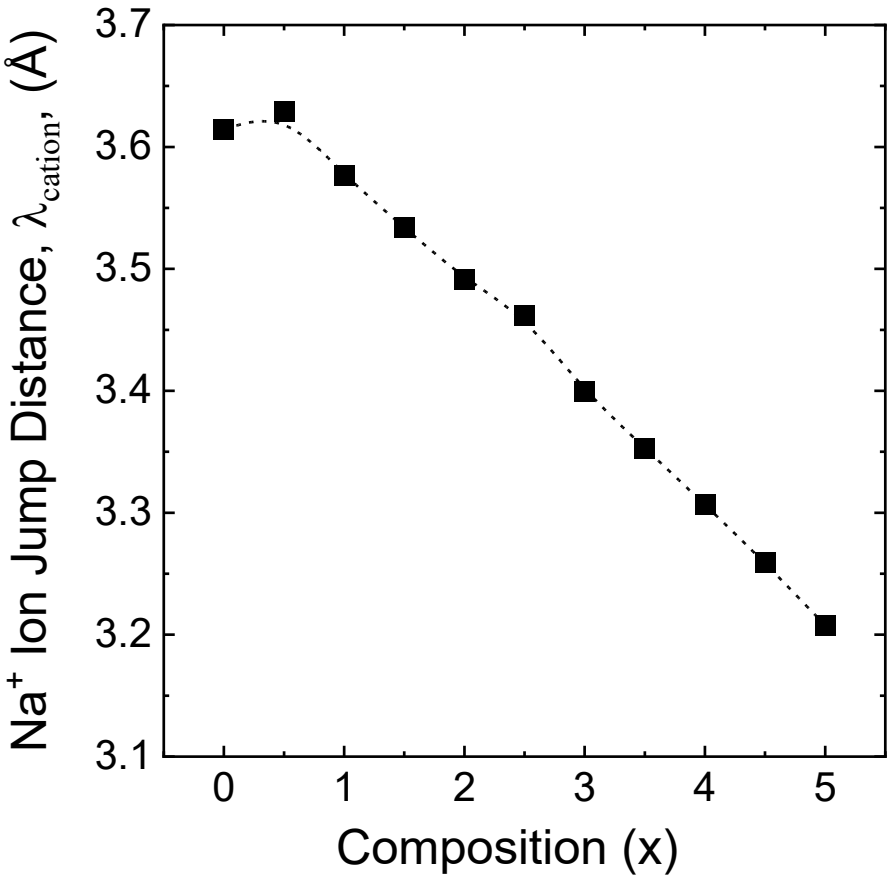

Figure 8. Composition dependence of the average Na^+ jump distance, λ_{cation}, determined from the anion distribution in and the molar volume of the glasses. With increasing x, the jump distance decreases as the result of a denser glass network arising from the small oxygen anions.

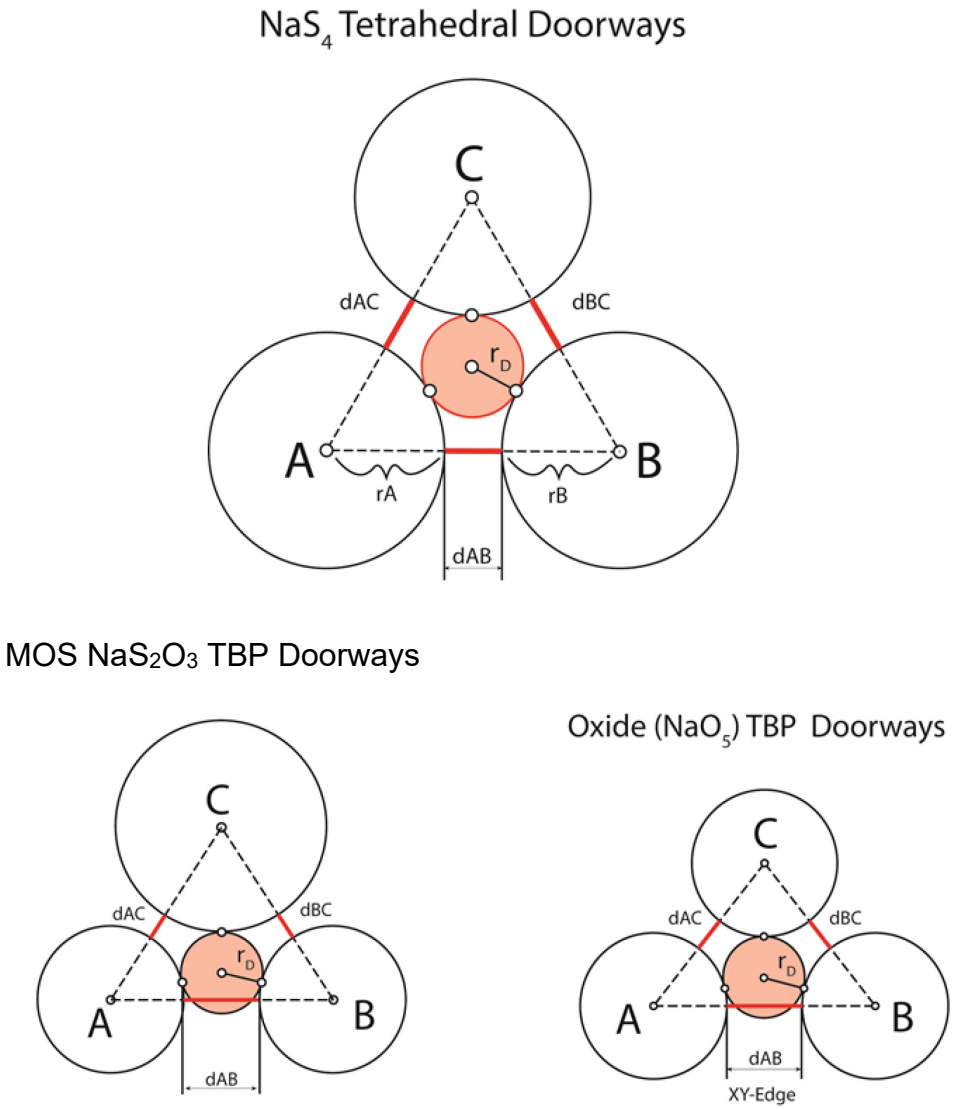

Figure 9. Two dimensional depictions of the geometric models for the r_D doorway analysis. (Top) The NaS_4 T site with a doorway of 3 sulfur atoms, showing a much larger doorway though the face than the edges of the T site. (Left) The $NaSO_4$ TBP site with a window consisting of 1 sulfur atom (Vert) and 2 oxygen atoms (XY-edge). The vertical edge (dAC and dBC) exhibits a contracted doorway due to the higher CN and thus it is proposed, see text, that the Na^+ ions prefer to jump via the face or XY edge in the NaX_5 MOS sites. (Right) The NaO_5 site with a window consisting of 3 oxygen atoms, showing a much larger doorway though the face and XY- edges compared to that of the vertical edges.

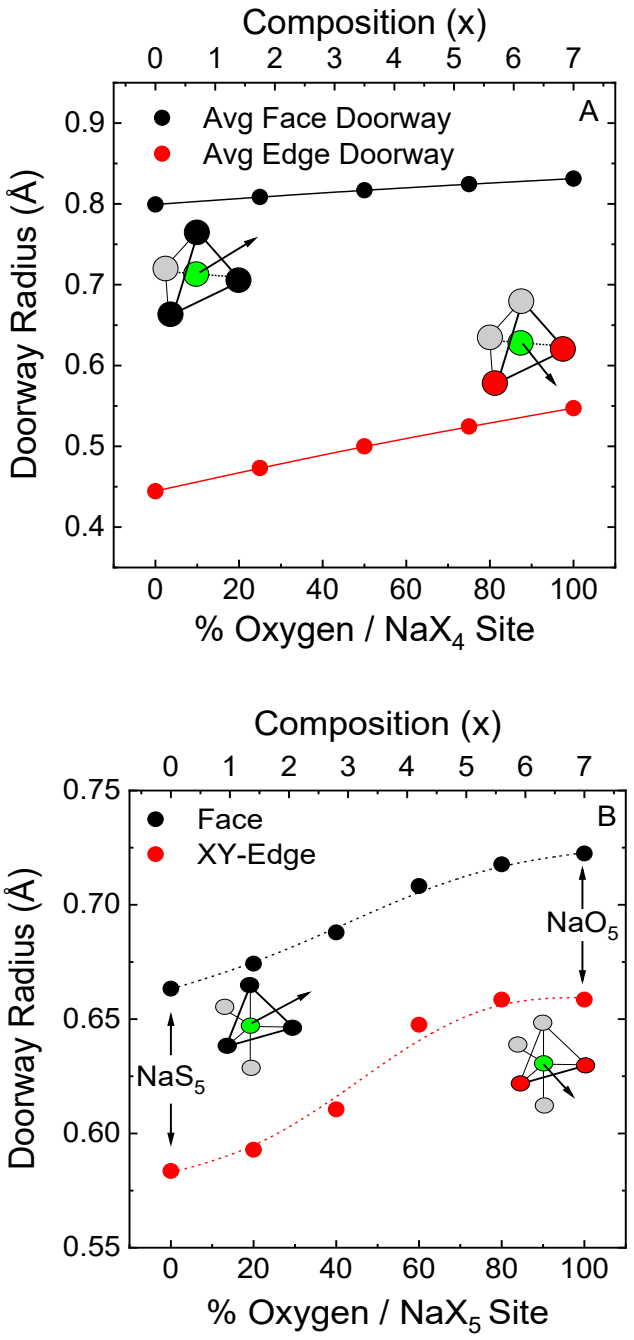

Figure 10. A. Composition dependence of the calculated face and edge doorway radii, r_D, for the proposed NaX_4 T environments showing that both values increase nearly linearly with the addition of oxygen. B. Composition dependence of the calculated face and XY-edge doorway radii, r_D, for proposed NaX_5 TBP environments showing a sigmoidal increase in both values with the addition of oxygen.

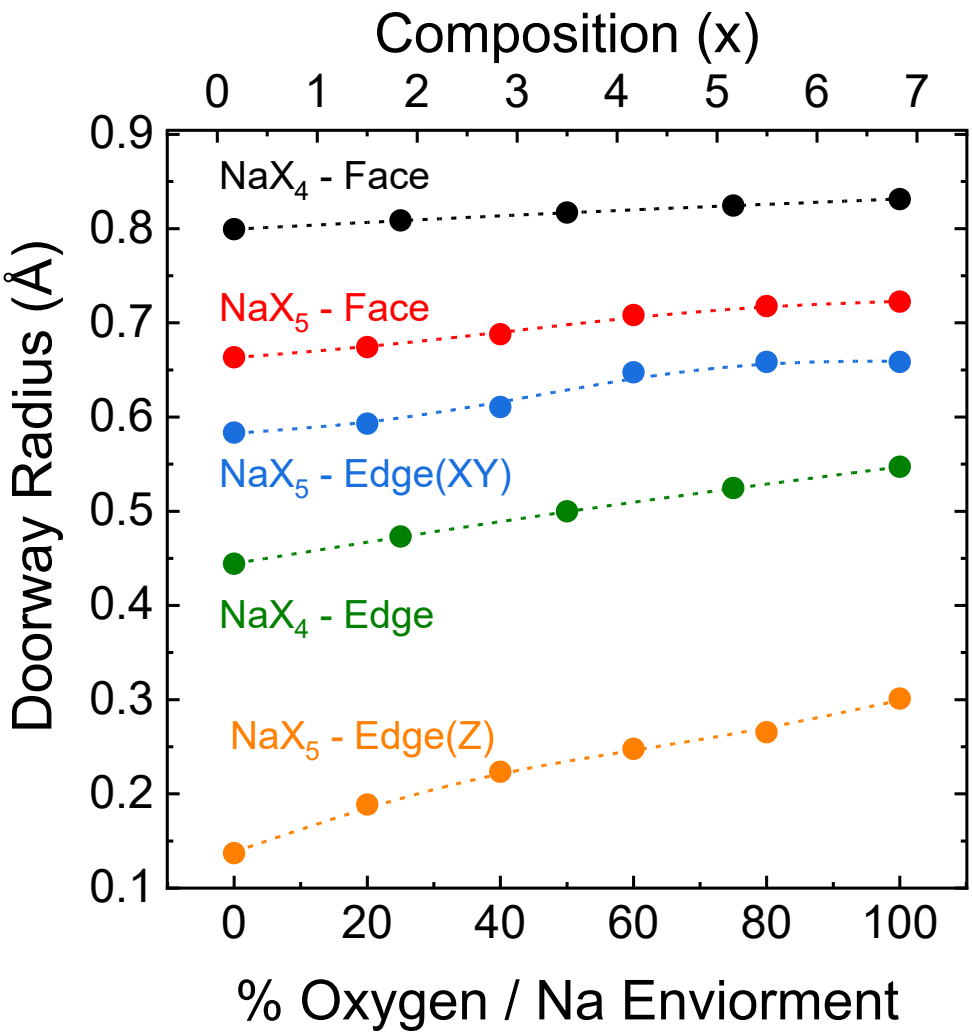

Figure 11. Comparisons of the calculated doorway radii, r_D, for all of the NaX_4 and NaX_5 MOS environments. Both the face and edge doorway radii were calculated from geometric models of the sites using a numerical solution to the Apollonius theorem, see text.

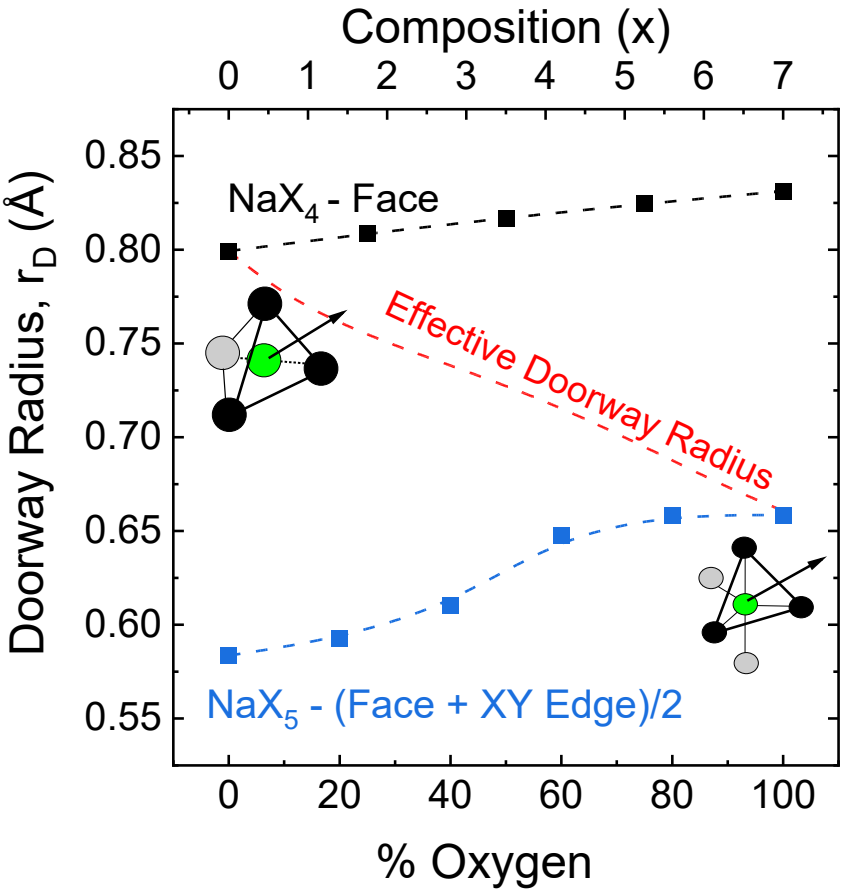

Figure 12. Proposed composition dependence of the doorway radius, r_D, assuming the largest physically reasonable doorways that in turn would result in the lowest strain energies, ΔE_S. Here, a linear exchange between NaX_4 – Face, and the average NaX_5 – (Face + XY(Edge))/2 doorway radii is assumed to account for the coordination number change. Here it is expected that for the x = 0 pure sulfide glass, all of the Na are expected to be coordinated in NaS_4 T environments whereas for the x = 7 pure oxide, all of the Na are expected to be coordinated in NaO_5 TBP environments.

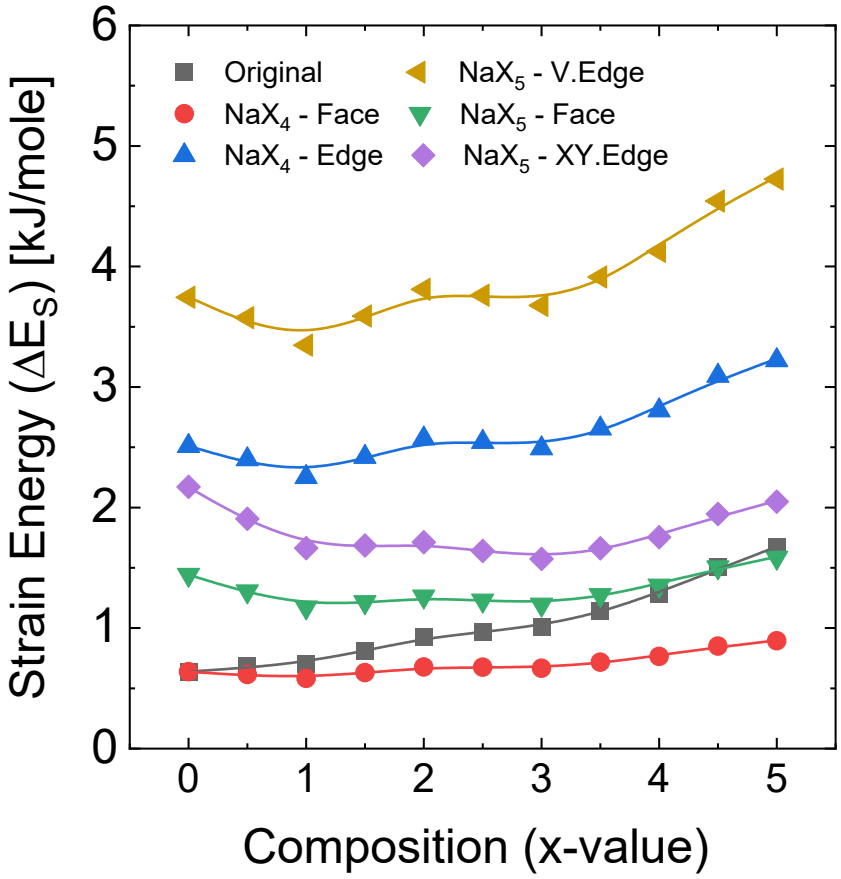

Figure 13. Strain energy contribution as determined by the different jump paths (doorway radii) of the investigated NaX_4 and NaX_5 site geometries.

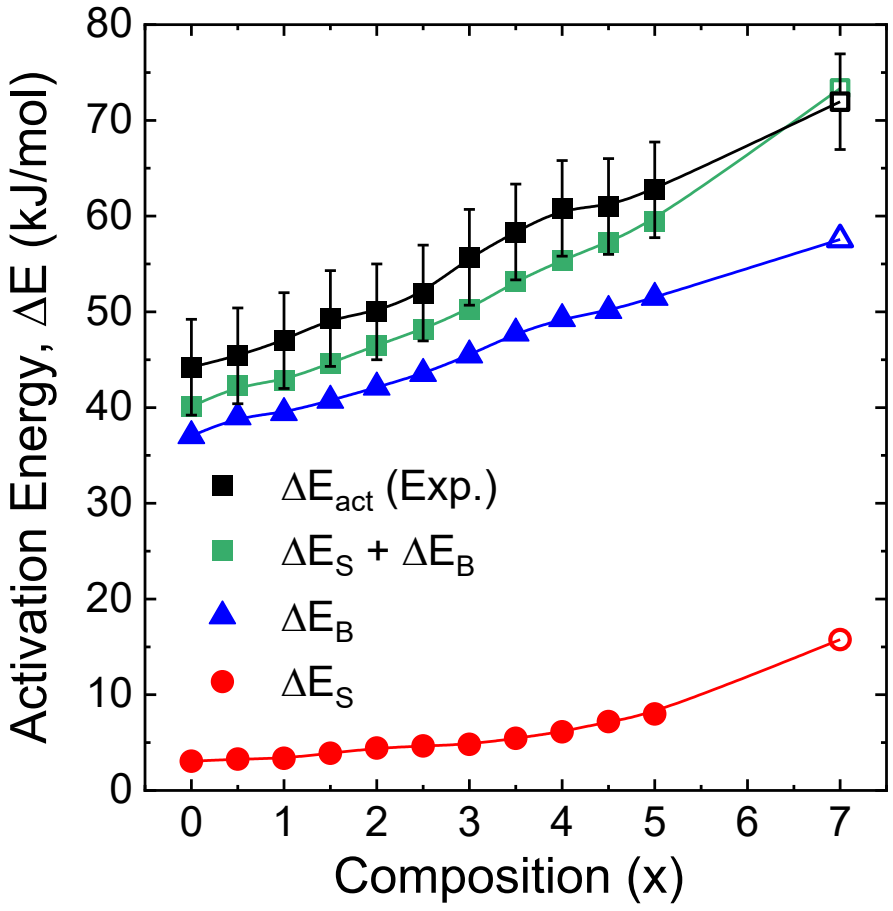

Figure 14. Calculated composition dependence of the strain energy, ΔE_S, based on the effective doorway radius, Fig. 12, Calculated composition dependence of the binding energy, ΔE_B, and the sum $\Delta E_B + \Delta E_S$ compared to the experimentally measured ΔE_{act} values. The model calculated sum agrees exceptionally well with and within the experimental error of the experimentally determined values. Open symbols refer to the calculated and measured values for the polycrystalline ceramic x = 7, $Na_4P_2O_7$.

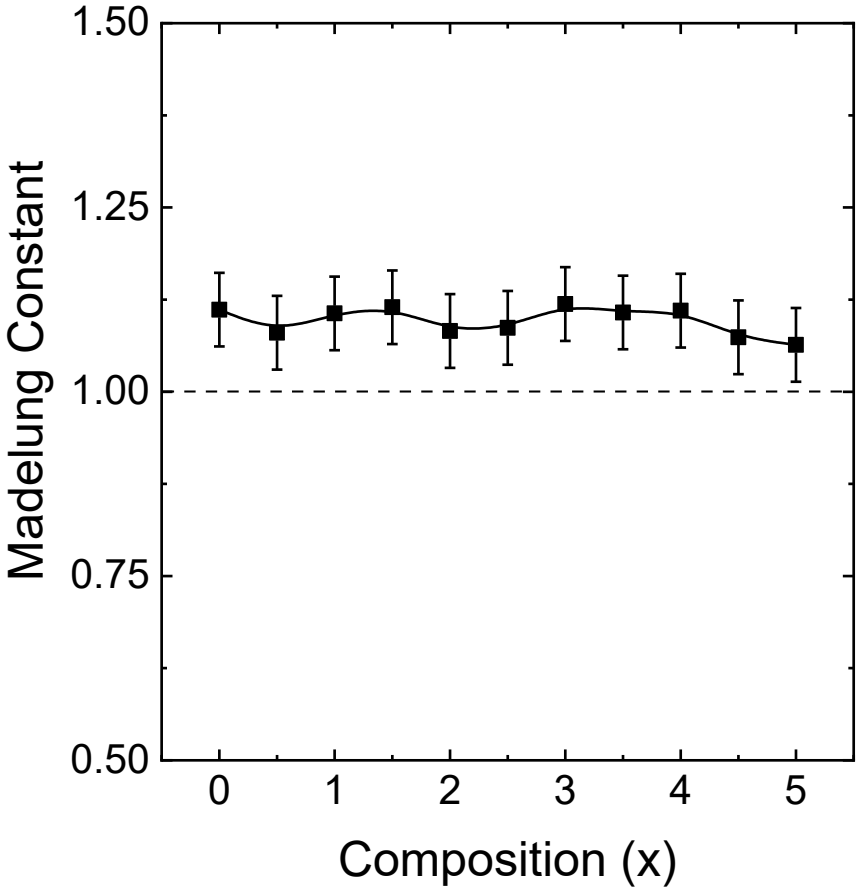

Figure 15. Calculated composition dependent Madelung constant, M_C, for the $Na_4P_2S_{7-x}O_x$ glasses from the calculated total of ΔE_B and ΔE_S and the measured activation energy ΔE_{act}, see text. The value of near unity shows that the model calculated total activation energy agrees well with the experimentally determined conductivity activation energy. Such agreement suggests that the many body effects of the coulomb potential appears to well be described by the limiting high frequency ε_∞ values, Fig. 8 B.

References

(1) Ye, H.; Wang, C.-Y.; Zuo, T.-T.; Wang, P.-F.; Yin, Y.-X.; Zheng, Z.-J.; Wang, P.; Cheng, J.; Cao, F.-F.; Guo, Y.-G. Realizing a highly stable sodium battery with dendrite-free sodium metal composite anodes and O3-type cathodes. *Nano Energy* **2018,** *48*, 369-376.
(2) Cohn, A. P.; Metke, T.; Donohue, J.; Muralidharan, N.; Share, K.; Pint, Cary L. Rethinking sodium-ion anodes as nucleation layers for anode-free batteries. *Journal of Materials Chemistry A* **2018,** *6* (46), 23875-23884.
(3) Cohn, A. P.; Muralidharan, N.; Carter, R.; Share, K.; Pint, C. L. Anode-Free Sodium Battery through in Situ Plating of Sodium Metal. *Nano Letters* **2017,** *17* (2), 1296-1301.
(4) Yabuuchi, N.; Komaba, S. Recent research progress on iron- and manganese-based positive electrode materials for rechargeable sodium batteries. *Sci. Technol. Adv. Mater.* **2014,** *15* (4), 043501/1-043501/29, 29 pp.
(5) Hayashi, A.; Noi, K.; Tanibata, N.; Nagao, M.; Tatsumisago, M. High sodium ion conductivity of glass–ceramic electrolytes with cubic Na3PS4. *Journal of Power Sources* **2014,** *258*, 420-423.
(6) Palomares, V.; Casas-Cabanas, M.; Castillo-Martinez, E.; Han, M. H.; Rojo, T. Update on Na-based battery materials. A growing research path. *Energy & Environmental Science* **2013,** *6* (8), 2312-2337.
(7) Hayashi, A.; Noi, K.; Sakuda, A.; Tatsumisago, M. Superionic glass-ceramic electrolytes for room-temperature rechargeable sodium batteries. *Nature Communications* **2012,** *3* (May), 1843/1-1843/5.
(8) Feng, X.; Chien, P.-H.; Zhu, Z.; Chu, I.-H.; Wang, P.; Immediato-Scuotto, M.; Arabzadeh, H.; Ong, S. P.; Hu, Y.-Y. Studies of Functional Defects for Fast Na-Ion Conduction in Na3−yPS4−xClx with a Combined Experimental and Computational Approach. *Advanced Functional Materials* **2019,** *29* (9), 1807951.
(9) Han, F.; Westover, A. S.; Yue, J.; Fan, X.; Wang, F.; Chi, M.; Leonard, D. N.; Dudney, N. J.; Wang, H.; Wang, C. High electronic conductivity as the origin of lithium dendrite formation within solid electrolytes. *Nature Energy* **2019,** *4* (3), 187-196.
(10) Porz, L.; Swamy, T.; Sheldon, B. W.; Rettenwander, D.; Frömling, T.; Thaman, H. L.; Berendts, S.; Uecker, R.; Carter, W. C.; Chiang, Y.-M. Mechanism of Lithium Metal Penetration through Inorganic Solid Electrolytes. *Advanced Energy Materials* **2017,** *7* (20), 1701003.
(11) Richards, W. D.; Miara, L. J.; Wang, Y.; Kim, J. C.; Ceder, G. Interface Stability in Solid-State Batteries. *Chemistry of Materials* **2016,** *28* (1), 266-273.
(12) Hayashi, A.; Tatsumisago, M. Development of ion conducting glasses for all-solid-state batteries. *Kagaku Kogyo* **2012,** *63* (10), 770-774.
(13) Hayashi, A.; Tatsumisago, M. Development of solid electrolytes with sodium ion conductivity for application to all-solid-state batteries. *Mater. Integr.* **2012,** *25* (1), 17-21.
(14) Wen, Z.; Hu, Y.; Wu, X.; Han, J.; Gu, Z. Main Challenges for High Performance NAS Battery: Materials and Interfaces. *Advanced Functional Materials* **2013,** *23* (8), 1005-1018.
(15) Qiu, G.; Liu, P.; Zeng, L.; Liao, W.; Liu, X. Development of sodium-sulfur battery. *Cailiao Daobao* **2011,** *25* (11a), 34-37, 65.
(16) Lu, X.; Lemmon, J. P.; Sprenkle, V.; Yang, Z. Sodium-beta alumina batteries: Status and challenges. *JOM* **2010,** *62* (9), 31-36.

(17) Oshima, T.; Okuno, A.; Totoki, T.; Mima, T. Development and commercialization of sodium-sulfur batteries applying β-alumina ceramics. *Seramikkusu* **2005,** *40* (8), 656-657.
(18) Dustmann, C. H. Beta ceramic in ZEBRA and NAS batteries. *Ceram.Mater.Compon.Engines, [Int.Symp.], 7th* **2001,** (12005-16-2 (Aluminum sodium oxide (Al5NaO8) Role: DEV (Device component use), USES (Uses) (beta "-alumina electrolyte for Na-S and ZEBRA batteries)), 33-37.
(19) Hayashi, A. Preparation of Li2S–P2S5 Amorphous Solid Electrolytes by Mechanical Milling. *Journal of the American Ceramic Society* **2016,** *84* (2), 477-79.
(20) Tatsumisago, M. Formation of Li+ superionic crystals from the Li2S–P2S5 melt-quenched glasses | SpringerLink. **2016**.
(21) Ohtomo, T.; Hayashi, A.; Tatsumisago, M.; Tsuchida, Y.; Hama, S.; Kawamoto, K. All-solid-state lithium secondary batteries using the 75Li2S·25P2S5 glass and the 70Li2S·30P2S5 glass-ceramic as solid electrolytes. *J. Power Sources* **2013,** *233*, 231-235.
(22) Martin, S. W., Glass and Glass-Ceramic Sulfide and Oxy-Sulfide Solid Electrolytes. In *Handbook of Solid State Batteries, 2nd Edition*, Dudney, N.; West, W.; Nanda, J., Eds. World Scientific: New Jersey, 2015; pp 433-501.
(23) Tuller, H. L.; Barsoum, M. W. Glass solid electrolytes: past, present and near future - the year 2004. *J.Non-Cryst.Solids* **1985,** *73, 331-50*.
(24) Tuller, H. L.; Button, D. P.; Uhlmann, D. R. Fast ion transport in oxide glasses. *Journal of Non-Crystalline Solids* **1980,** *40*, 93-118.
(25) Martin, S. W.; Bischoff, C.; Schuller, K. Composition Dependence of the Na+ Ion Conductivity in 0.5Na2S + 0.5[xGeS2 + (1 - x)PS5/2] Mixed Glass Former Glasses: A Structural Interpretation of a Negative Mixed Glass Former Effect. *J. Phys. Chem. B* **2015,** *119* (51), 15738-15751.
(26) Schuch, M.; Mueller, C. R.; Maass, P.; Martin, S. W. Mixed Barrier Model for the Mixed Glass Former Effect in Ion Conducting Glasses. *Phys.Rev.Lett.* **2009,** *102* (14), 145902/1-145902/4.
(27) Schuch, M.; Trott, C.; Maass, P. Network forming units in alkali borate and borophosphate glasses and the mixed glass former effect. *RSC Advances* **2011,** *1* (7), 1370-1382.
(28) Klein, R. J.; Zhang, S.; Dou, S.; Jones, B. H.; Colby, R. H.; Runt, J. Modeling electrode polarization in dielectric spectroscopy: Ion mobility and mobile ion concentration of single-ion polymer electrolytes. *The Journal of Chemical Physics* **2006,** *124* (14), 144903.
(29) Bischoff, C.; Schuller, K.; Beckman, S. P.; Martin, S. W. Non-Arrhenius ionic conductivities in glasses due to a distribution of activation energies. *Phys. Rev. Lett.* **2012,** *109* (7), 075901/1-075901/4.
(30) Kmiec, S.; Joyce, A.; Bayko, D.; Martin, S. W. Glass formation and structure of melt quenched mixed oxy-sulfide Na4P2S7-xOx glasses for $0 \leq x \leq 5$. *Journal of Non-Crystalline Solids* **2020,** *534*, 119776.
(31) Shannon, R. D. Revised effective ionic radii and systematic studies of interatomic distances in halides and chalcogenides. *Acta Crystallogr., Sect. A* **1976,** *A32* (5), 751-67.
(32) Nose, M.; Kato, A.; Sakuda, A.; Hayashi, A.; Tatsumisago, M. Evaluation of Mechanical Properties of Na2S-P2S5 Sulfide Glass Electrolytes. *Journal of Materials Chemistry A: Materials for Energy and Sustainability* **2015,** *3* (Li), 22061-22065.

(33) Bischoff, C.; Schuller, K.; Martin, S. W. Short Range Structural Models of the Glass Transition Temperatures and Densities of 0.5Na2S + 0.5[xGeS2 + (1 - x)PS5/2] Mixed Glass Former Glasses. *J. Phys. Chem. B* **2014,** *118* (13), 3710-3719.
(34) Schrödter, K.; Bettermann, G.; Staffel, T.; Wahl, F.; Klein, T.; Hofmann, T., Phosphoric Acid and Phosphates. In *Ullmann's Encyclopedia of Industrial Chemistry*, 2008.
(35) Le Messurier, D.; Petkov, V.; Martin, S. W.; Kim, Y.; Ren, Y. Three-dimensional structure of fast ion conducting 0.5Li2S+0.5[(1- x)GeS2 + xGeO2] glasses from high-energy X-ray diffraction and reverse Monte Carlo simulations. *J.Non-Cryst.Solids* **2009,** *355* (7), 430-437.
(36) Kim, Y.; Saienga, J.; Martin, S. W. Anomalous Ionic Conductivity Increase in Li2S + GeS2 + GeO2 Glasses. *Journal of Physical Chemistry B* **2006,** *110* (33), 16318-16325.
(37) Kim, Y.; Saienga, J.; Martin, S. W. Preparation and characterization of germanium oxy-sulfide GeS2–GeO2 glasses. *Journal of Non-Crystalline Solids* **2005,** *351* (24–26), 1973-1979.
(38) Bhide, A.; Hariharan, K. Sodium ion transport in NaPO3–Na2SO4 glasses. *Materials Chemistry and Physics* **2007,** *105* (2), 213-221.
(39) Dikshit, U. C.; Kumar, M. Analysis of Electronic Polarizabilities in Ionic Crystals. *physica status solidi (b)* **1991,** *165* (2), 599-610.
(40) Kmiec, S.; Joyce, A.; Martin, S. W. Glass formation and structural analysis of Na4P2S7-xOx, $0 \leq x \leq 7$ sodium oxy-thiophosphate glasses. *Journal of Non-Crystalline Solids* **2018,** *498*, 177-189.
(41) Kmiec, S. J.; Lovi, J. M.; Joyce, A.; Bayko, D.; Martin, S. W. Anomalously strong viscosity behavior in mixed oxy-sulfide Na4P2S7-xOx invert glasses. *Journal of Non-Crystalline Solids* **2021,** *553*, 120493.
(42) Jansen, M.; Henseler, U. Synthesis, structure determination, and ionic conductivity of sodium tetrathiophosphate. *Journal of Solid State Chemistry* **1992,** *99* (1), 110-119.
(43) Christensen, R.; Olson, G.; Martin, S. W. Ionic Conductivity of Mixed Glass Former 0.35Na2O + 0.65[xB2O3 + (1 - x)P2O5] Glasses. *J. Phys. Chem. B* **2013,** *117* (51), 16577-16586.
(44) Kim, Y.; Saienga, J.; Martin, S. W. Anomalous Ionic Conductivity Increase in Li2S + GeS2 + GeO2 Glasses. *J.Phys.Chem.B* **2006,** *110* (33), 16318-16325.
(45) Dietrich, C.; Weber, D. A.; Sedlmaier, S. J.; Indris, S.; Culver, S. P.; Walter, D.; Janek, J.; Zeier, W. G. Lithium ion conductivity in Li2S–P2S5 glasses – building units and local structure evolution during the crystallization of superionic conductors Li3PS4, Li7P3S11 and Li4P2S7. *Journal of Materials Chemistry A* **2017,** *5* (34), 18111-18119.
(46) Calahoo, C.; Wondraczek, L. Ionic glasses: Structure, properties and classification. *Journal of Non-Crystalline Solids: X* **2020,** *8*, 100054.
(47) Anderson, O. L.; Stuart, D. A. Calculation of activation energy of ionic conductivity in silica glasses by classical methods. *J.Am.Ceram.Soc.* **1954,** *37* (12), 574-580.
(48) Martin, S. W.; Christensen, R.; Olson, G.; Kieffer, J.; Wang, W. New Interpretation of Na+-Ion Conduction in and the Structures and Properties of Sodium Borosilicate Mixed Glass Former Glasses. *J. Phys. Chem. C* **2019,** *123* (10), 5853-5870.
(49) McElfresh, D. K.; Howitt, D. G. Activation enthalpy for diffusion in glass. *Journal of the American Ceramic Society* **1986,** *69* (10), C237-C238.
(50) Hall, A.; Swenson, J.; Karlsson, C.; Adams, S.; Bowron, D. T. Structure of AgxNa1-xPO3 glasses by neutron diffraction and reverse Monte Carlo modelling. *J.Phys.: Condens.Matter* **2007,** *19* (41), 415115/1-415115/9.

(51) Beaufils, S.; Cormier, L.; Bionducci, M.; Ecolivet, C.; Calas, G.; Le Sauze, A.; Marchand, R. Medium-range order in alkali metaphosphate glasses and melts investigated by reverse Monte Carlo simulations and diffraction analysis. *Physical Review B: Condensed Matter and Materials Physics* **2003,** *67* (10), 104201/1-104201/7.
(52) Hoppe, U.; Stachel, D.; Beyer, D. The oxygen coordination of metal ions in phosphate and silicate glasses studied by a combination of x-ray and neutron diffraction. *Physica Scripta, T* **1995,** *T57* (Neutrons in Disordered Matter), 122-126.
(53) Harpale, A. Problem of Apollonius. *MATLAB Central File Exchange.* **2020**.
(54) Frenkel, J., *Kinetic Theory of Liquids*. Peter Smith Publisher, Incorporated: 1984.
(55) Souquet, J. L.; Perera, W. G. Thermodynamics applied to ionic transport in glasses. *Solid State Ionics* **1990,** *40/41*, 595-604.
(56) Ravaine, D. Ionic transport properties in glasses. *Journal of Non-Crystalline Solids* **1985,** *73*, 287-303.
(57) Ingram, M. D.; Moynihan, C. T.; Lesikar, A. V. Ionic conductivity and the weak electrolyte theory of glass. *J.Non-Cryst.Solids* **1980,** *38-39, 371-6*.
(58) Cruguel, H.; Guittet, M. J.; Kerjan, O.; Bart, F.; Gautier-Soyer, M. Bonding and chemical shifts in aluminosilicate glasses: importance of Madelung effects. *J. Electron Spectrosc. Relat. Phenom.* **2003,** *128* (2-3), 271-278.
(59) Cooper, A. R. Zachariasen's rules, Madelung constant, and network topology. *Phys. Chem. Glasses* **1978,** *19* (4), 60-8.
(60) Izgorodina, E. I.; Bernard, U. L.; Dean, P. M.; Pringle, J. M.; MacFarlane, D. R. The Madelung Constant of Organic Salts. *Cryst. Growth Des.* **2009,** *9* (11), 4834-4839.
(61) de Jong, M.; Chen, W.; Angsten, T.; Jain, A.; Notestine, R.; Gamst, A.; Sluiter, M.; Krishna Ande, C.; van der Zwaag, S.; Plata, J. J.; Toher, C.; Curtarolo, S.; Ceder, G.; Persson, K. A.; Asta, M. Charting the complete elastic properties of inorganic crystalline compounds. *Scientific Data* **2015,** *2* (1), 150009.
(62) Jain, A.; Ong, S. P.; Hautier, G.; Chen, W.; Richards, W. D.; Dacek, S.; Cholia, S.; Gunter, D.; Skinner, D.; Ceder, G.; Persson, K. A. Commentary: The Materials Project: A materials genome approach to accelerating materials innovation. *APL Materials* **2013,** *1* (1), 011002.